Cellular/Molecular

Hyperexcitability and Hyperplasticity Disrupt Cerebellar Signal Transfer in the *IB2* KO Mouse Model of Autism

Teresa Soda,[1,3]* Lisa Mapelli,[1]* Francesca Locatelli,[1] Laura Botta,[2] Mitchell Goldfarb,[4] Francesca Prestori,[1] and Egidio D'Angelo[1,5]****

Departments of [1]Brain and Behavioral Sciences, [2]Biology and Biotechnology "L. Spallanzani," University of Pavia, 27100 Pavia, Italy, [3]Museo Storico della Fisica e Centro Studi e Ricerche Enrico Fermi, 00184 Rome, Italy, [4]Department of Biological Sciences, Hunter College, New York, New York 10065, and [5]Brain Connectivity Center, C. Mondino National Neurological Institute, 27100 Pavia, Italy

Autism spectrum disorders (ASDs) are pervasive neurodevelopmental conditions that often involve mutations affecting synaptic mechanisms. Recently, the involvement of cerebellum in ASDs has been suggested, but the underlying functional alterations remained obscure. We investigated single-neuron and microcircuit properties in IB2 (Islet Brain-2) KO mice of either sex. The IB2 gene (chr22q13.3 terminal region) deletion occurs in virtually all cases of Phelan–McDermid syndrome, causing autistic symptoms and a severe delay in motor skill acquisition. IB2 KO granule cells showed a larger NMDA receptor-mediated current and enhanced intrinsic excitability, raising the excitatory/inhibitory balance. Furthermore, the spatial organization of granular layer responses to mossy fibers shifted from a "Mexican hat" to a "stovepipe hat" profile, with stronger excitation in the core and weaker inhibition in the surround. Finally, the size and extension of long-term synaptic plasticity were remarkably increased. These results show for the first time that hyperexcitability and hyperplasticity disrupt signal transfer in the granular layer of IB2 KO mice, supporting cerebellar involvement in the pathogenesis of ASD.

Key words: **autism; cerebellum; excitatory/inhibitory balance; hyperplasticity; NMDA receptor**

Significance Statement

This article shows for the first time a complex set of alterations in the cerebellum granular layer of a mouse model [IB2 (Islet Brain-2) KO] of autism spectrum disorders. The IB2 KO in mice mimics the deletion of the corresponding gene in the Phelan–McDermid syndrome in humans. The changes reported here are centered on NMDA receptor hyperactivity, hyperplasticity, and hyperexcitability. These, in turn, increase the excitatory/inhibitory balance and alter the shape of center/surround structures that emerge in the granular layer in response to mossy fiber activity. These results support recent theories suggesting the involvement of cerebellum in autism spectrum disorders.

Introduction

Autism spectrum disorders (ASDs) are pervasive developmental disorders characterized by impairment in social communication and social interaction and by the presence of repetitive behaviors and/or restricted interests. ASDs cover a spectrum of different clinical conditions ranging from severely hypofunctional to hyperfunctional, and show abnormalities in different brain regions. Although most attention has been given so far to the cerebral cortex, increasing evidence also implicates the cerebellum (Amaral, 2011; Betancur, 2011; Ellegood et al., 2015). Cerebellar lesions often cause autistic-like symptoms (Hampson and Blatt, 2015), and perinatal cerebellar injuries are the greatest nongenetic risk factor for ASDs (Bolduc and Limperopoulos, 2009; Limperopoulos et al., 2009; Bolduc et al., 2011; Wang et al., 2014; Mosconi et al., 2015). Moreover, cerebellar alterations are found in several syndromic forms of ASDs, like Phelan–McDermid, Fragile X, Tuberous Sclerosis, and Rett syndrome (for review, see Courchesne and Allen, 1997; Schmahmann, 2004; Allen, 2006; Ito, 2008; D'Angelo and Casali, 2013; Broussard, 2014; Hampson and Blatt, 2015; Mosconi et al., 2015; Zeidán-Chuliá et al., 2016). This raises a main question: are there any alterations of cerebellar microcircuit functions in ASDs?

ASDs are often associated with mutations in genes coding for synaptic proteins (Qiu et al., 2012; Banerjee et al., 2014; De Ru-

Received July 27, 2018; revised Dec. 22, 2018; accepted Jan. 8, 2019.

Author contributions: M.G. and E.D. designed research; T.S., L.M., F.L., L.B., and F.P. performed research; M.G. contributed unpublished reagents/analytic tools; T.S., L.M., and F.P. analyzed data; L.M., F.P., and E.D. wrote the paper.

This project has received funding from the European Union's Horizon 2020 Framework Program for Research and Innovation under Grant Agreement No. 720270 (Human Brain Project SGA1); European Union grant Human Brain Project (HBP-604102) to E.D.; a Fermi Grant CNL to E.D.; and Blue-Sky Research Grant of the University of Pavia (BSR77992) to L.M. We thank Simona Tritto for technical assistance.

*T.S. and L.M. are co-first authors.

**F.P. and E.D. are co-last authors.

The authors declare no competing financial interests.

Correspondence should be addressed to Egidio D'Angelo at dangelo@unipv.it.

https://doi.org/10.1523/JNEUROSCI.1985-18.2019

 0270-6474/19/392383-15$15.00/0

beis and Buxbaum, 2015; Kim et al., 2016) bringing about neurotransmission abnormalities (Curatolo et al., 2014; Ellegood et al., 2015; Kloth et al., 2015; Mercer et al., 2016; Sztainberg and Zoghbi, 2016; Tsai, 2016; Tu et al., 2017). The consequent microcircuit alterations have mainly been analyzed in the neocortex revealing the following: (1) hyper-reactivity to stimulation, accompanied by altered neuronal excitability and synaptic plasticity, was related to increased glutamatergic transmission (Rinaldi et al., 2007, 2008b; Markram et al., 2008; Markram and Markram, 2010); (2) dysregulation of the excitation (E)/inhibition (I) balance was related to various alterations at excitatory and inhibitory synapses (Rubenstein and Merzenich, 2003; Gogolla et al., 2009; Uzunova et al., 2016); and (3) altered modular organization of microcircuits (Casanova, 2003, 2006; Hutsler and Casanova, 2016) was related to reduced lateral inhibition, bringing about changes in the spatial organization of neuronal activation and synaptic plasticity. In particular, center/surround (C/S) structures were proposed to change from a "Mexican hat" to a "stovepipe hat" profile (Casanova, 2006).

A key role in synaptic and microcircuit dysregulation has been suggested by NMDA receptor hyperfunction (Rinaldi et al., 2007). Important for the present case, NMDA receptor-mediated currents were increased in cerebellar granule cells of the IB2 (Islet Brain-2) knock-out (KO) mouse. These mice have a range of behavioral deficits reminiscent of Phelan–McDermid syndrome and ASDs (Phelan et al., 2001; Manning et al., 2004; Soorya et al., 2013; Kolevzon et al., 2014), in which autistic symptoms are associated with cerebellar functional deficits, including severely impaired motor performance and learning (Giza et al., 2010). IB2 (MAPK8IP2) is a scaffolding protein enriched in the PSD, probably regulating signal transduction by protein kinase cascades, that operates inside the NMDA receptor interactome (Yasuda et al., 1999). Since NMDA receptor expression in granule cells is the highest among cerebellar neurons (Monaghan and Cotman, 1985) and has a profound impact on synaptic excitation and plasticity (D'Angelo et al., 1995; Armano et al., 2000; Sola et al., 2004; D'Errico et al., 2009), IB2 KO mice actually provide an ideal model to investigate cerebellar microcircuit alterations in ASD. In the cerebellar granular layer, granule cells receive excitatory synapses from mossy fibers and are inhibited by Golgi cells. The synaptic interaction between these neurons forms the granular layer microcircuit, which, once activated by incoming spike bursts, generates responses organized in C/S (Mapelli and D'Angelo, 2007; Gandolfi et al., 2014). Here we show that the granular layer of IB2 KO mice is characterized by hyperexcitability and hyperplasticity, which raise the E/I balance disrupting C/S structures and signal transfer at the input stage of cerebellum. The implications of these cerebellar microcircuit alterations for ASD pathogenesis are discussed.

Materials and Methods

All procedures were conducted in accordance with European Guidelines for the Care and Use of Laboratory Animals (Council Directive 2010/63/EU) and approved by the Ethical Committee of Italian Ministry of Health (637/2017-PR).

Genotyping and maintenance of IB2 KO mice. Experiments were conducted on $IB2^{+/+}$ [wild-type (WT)] and $IB2^{-/-}$ (KO) mice obtained by crossing $IB2^{+/-}$ parents, since IB2 KO are poor breeders, possibly reflecting the social deficit associated with IB2 deletion (Giza et al., 2010). The genotyping was conducted through PCR using four primers to detect wild-type and null alleles, as previously described (Giza et al., 2010).

Slice preparation and solutions. The experiments reported in this article have been conducted on 17- to 24-d-old (postnatal day 0 = day of birth) WT and IB2 KO mice of either sex. Mice were anesthetized with halothane (Sigma-Aldrich) and killed by decapitation to remove the cerebellum for acute slice preparation according to a well established technique (D'Angelo et al., 1995; Armano et al., 2000; Gall et al., 2005; Prestori et al., 2013; Nieus et al., 2014). The vermis was isolated and fixed on the stage of the vibroslicer (model VT1200S, Leica) with cyano-acrylic glue. Acute 220-μm-thick slices were cut in the parasagittal plane in ice-cold (2–3°C) Krebs' solution containing the following (in mM): 120 NaCl, 2 KCl, 1.2 $MgSO_4$, 26 $NaHCO_3$, 1.2 KH_2PO_4, 2 $CaCl_2$, and 11 glucose, equilibrated with 95% O_2-5% CO_2, pH 7.4. Slices were allowed to recover at room temperature for at least 1 h, before being transferred to a recording chamber mounted on the stage of an upright microscope (Zeiss). The slices were perfused with oxygenated Krebs' solution and maintained at 32°C with a Peltier feedback device (catalog #TC-324B, Warner Instruments). Moreover, bath perfusion with Krebs' solution was commenced before seal formation and was maintained until the end of recording. Unless otherwise stated, Krebs' solutions contained the $GABA_A$ receptor antagonist SR95531 (gabazine, 10 μM; Abcam; control condition). In some experiments, modified Krebs' solutions were either Mg^{2+} free, gabazine free, or contained drugs to block excitatory glutamate receptors [2,3-dihydroxy-6-nitro-7-sulfonyl-benzo[*f*]quinoxaline (NBQX; 10 μM), aminophosphonovalerate (APV; 50 μM), and 7-chlorokynurenic acid (50 μM)].

Experimental design: electrophysiological recordings. Whole-cell patch-clamp recordings were performed with Multiclamp 700B [−3 dB; cutoff frequency (fc),10 kHz], sampled with Digidata 1440A interface, and analyzed off-line with pClamp10 software (Molecular Devices). Patch pipettes were pulled from borosilicate glass capillaries (Sutter Instruments) and filled with different solutions depending on the specific experiments (see below). Mossy fiber stimulation was performed with a bipolar tungsten electrode (Clark Instruments) via a stimulus isolation unit. The stimulating electrode was placed over the central fiber bundle in the cerebellar lamina to stimulate the mossy fibers, and 200 μs step current pulses were applied at the frequency of 0.1–0.33 Hz (in specific experiments, paired-pulse stimulation at 20 ms interpulse was used). From a comparison with data reported previously (Sharma and Vijayaraghavan, 2003; Giza et al., 2010; Sgritta et al., 2017), one or two mossy fibers were stimulated per granule cell in the experiments used for quantal analysis. Long-term potentiation (LTP) induction was obtained by a continuous stimulation of 100 pulses at 100 Hz at −50 mV [high-frequency stimulation (HFS)], as reported previously (Armano et al., 2000; Gall et al., 2005; D'Errico et al., 2009; Prestori et al., 2013). The stability of whole-cell recordings can be influenced by the modification of series resistance (R_s). To ensure that R_s remained stable during recordings, passive electrode–cell parameters were monitored throughout the experiments. The granule cell behaves like a lumped electrotonic compartment and can therefore be treated as a simple resistive-capacitive system, from which relevant parameters can be extracted by analyzing passive current relaxation induced by step voltage changes. In each recording, once in the whole-cell configuration, the current transients elicited by 10 mV hyperpolarizing pulses from the holding potential of −70 mV in voltage-clamp mode showed a biexponential relaxation, with a major component related to a somatodendritic charging (Prestori et al., 2008). According to previous reports (D'Angelo et al., 1995, 1999; Silver et al., 1996), the major component was analyzed to extract basic parameters useful to evaluate the recording conditions and to compare different cell groups. Membrane capacitance (C_m) was measured from the capacitive charge (the area underlying current transients), and R_s was calculated as $R_s = \tau_{vc}/C_m$; τ = voltage-clamp time constant. The membrane resistance (R_m) was computed from the steady-state current flowing after termination of the transient. The 3 dB fc of the electrode-cell system was calculated as voltage-clamp cut-off frequency $(f_{vc}) = (2\pi \times \tau_{vc})^{-1}$. The data are reported in Table 1. In the cells considered for analysis, these values did not significantly change after 30 min, attesting to recording stability. Cells showing a variation of R_s of >20% were discarded from analysis.

Granule cell excitability. Patch pipettes had 7–9 MΩ resistance before seal formation with a filling solution containing the following (in mM): 126 potassium gluconate, 4 NaCl, 5 HEPES, 15 glucose, 1 $MgSO_4.7H_2O$, 0.1 BAPTA-free, 0.05 BAPTA-Ca^{2+}, 3 Mg^{2+}-ATP, and 0.1 Na^+-GTP, pH 7.2 adjusted with KOH. The calcium buffer is estimated to maintain a free calcium concentration of ~100 nM. Just after obtaining the cell-

Table 1. Properties of whole-cell recordings in mice granule cells

	WT ($n = 92$)	KO ($n = 76$)
R_m (GΩ)	2.0 ± 0.1	2.7 ± 0.2*
C_m (pF)	3.6 ± 0.1	3.2 ± 0.1***
R_s (MΩ)	17.6 ± 1.1	18.3 ± 1.0
f_{VC} (KHz)	3.5 ± 0.2	3.2 ± 0.2
V_m (mV)	−50.2 ± 1.4 ($n = 34$)	−49.2 ± 1.5 ($n = 30$)

V_m, Membrane potential. The data were obtained using K-gluconate intracellular solution and analyzing current transient elicited by 10 mV voltage-clamp steps delivered from the holding potential of −70 mV. The number of observations indicated and statistical significance are reported compared with IB2 KO granule cells.

*$p < 0.05$; ***$p < 0.001$, unpaired t test.

attached configuration, electrode capacitance was carefully cancelled to allow for electronic compensation of pipette charging during subsequent current-clamp recordings. At the beginning of each recording, a series of depolarizing steps was applied in voltage clamp to measure the total voltage-dependent current of the granule cell (Fig. 1*C*). Leakage and capacitance were subtracted using hyperpolarizing pulses delivered before the test pulse (P/4 protocol). After switching to current clamp, intrinsic excitability was investigated (Fig. 1*B*) by setting resting membrane potential at −80 mV and injecting 800 ms current steps (from −4 to 22 pA in 2 pA increment). The membrane potential during current steps was estimated as the average value between 600 and 800 ms. Action potential frequency was measured by dividing the number of spikes by step duration.

Postsynaptic currents. Patch pipettes had 5–8 MΩ resistance before seal formation with a filling solution containing the following (in mM): 81 Cs_2SO_4, 4 NaCl, 2 $MgSO_4$, 1 QX-314 (lidocaine *N*-ethyl bromide), 0.1 BAPTA-free and 0.05 BAPTA-Ca^{2+}, 15 glucose, 3 Mg^{2+}-ATP, 0.1 Na^+-GTP, and 15 HEPES, with pH adjusted to 7.2 with CsOH. The calcium buffer is estimated to maintain a free calcium concentration ~100 nM. Synaptic currents elicited at 0.1 Hz were averaged and digitally filtered at 1.5 kHz off-line. IPSC and EPSC peak amplitudes were taken at +10 and −70 mV to measure the $GABA_A$ and AMPA currents, respectively. In some experiments, NMDA current was directly measured at −70 mV in Mg^{2+}-free solution in the presence of the AMPA receptor blocker 10 μM NBQX (Sola et al., 2004). In LTP experiments, the acquisition program automatically alternated EPSC with background activity recordings (1 and 9 s, respectively), from which miniature EPSCs (mEPSCs) were detected. After 10 min (control period), the recording was switched to current clamp (patch pipettes were filled with a K^+-gluconate-based solution), and HFS was delivered to induce plasticity. Long-term synaptic efficacy changes were measured after 20 min. After delivering HFS, voltage clamp at −70 mV was re-established, and stimulation was restarted at the test frequency. EPSCs and mEPSCs were digitally filtered at 1.5 kHz and analyzed off-line with pClamp10 software (Molecular Devices). For both EPSC and mEPSC, the peak amplitude was computed. mEPSC detection was performed automatically with Mini Analysis Program (Synaptosoft) when their amplitude was five to seven times the baseline noise SD (S; 0.88 ± 0.03; $n = 8$). These criteria and a further visual inspection of detected signals allowed us to reject noise artifacts.

To investigate the expression mechanism of long-term synaptic plasticity over a heterogeneous dataset (Sola et al., 2004; Gall et al., 2005), a simplified version of quantal analysis was performed by measuring the mean (M) and S of EPSC amplitude. EPSC changes, which do not strictly require that single synaptic connections are isolated, were obtained from M and S: the coefficient of variation (CV) = S/M, the paired-pulse ratio (PPR) = M_2/M_1 (i.e., the ratio between the second and first EPSC amplitude in a doublet at a 20 ms interpulse interval). The comparison between M and CV obtained before and after the induction of plasticity could be performed in the plot $(CV_2/CVA_1)^{-2}$ versus (M_2/M_1). Assuming binomial statistics, this plot has the property that the unitary slope diagonal separates points caused by changes in quantum content ($m = np$, with n being the number of releasing sites and p the release probability) from those caused by changes in quantum size (q). The inequality leads to a topological representation of neurotransmission changes (see Fig. 7) and has been extensively used to interpret the plasticity mechanism (Bekkers and Stevens, 1990; Malinow and Tsien, 1990; Sola et al., 2004; Rinaldi et al., 2008b; D'Errico et al., 2009; Sgritta et al., 2017). For an M increase the following happens: (1) when $(CV_2/CVA_1)^{-2} > (M_2/M_1)$, both n and p can increase; (2) when $(CV_2/CVA_1)^{-2} = (M_2/M_1)$, only n can increase; and (3) when $(CV_2/CVA_1)^{-2} < (M_2/M_1)$, neither n nor p can increase, implying an increase in q. A pure increase in q will lie on the axis when $(CV_2/CVA_1)^{-2} = 1$.

Experimental design: voltage-sensitive dye imaging. The stock solution for voltage-sensitive dye imaging (VSDi) contained the dye Di-4-ANEPPS (Invitrogen) dissolved in a solution based on Krebs' solution containing 50% ethanol (Sigma-Aldrich) and 5% Cremophor EL (Sigma-Aldrich). Slices for optical recordings were incubated for 30 min in oxygenated Krebs' solution added to a 3% Di-4-ANEPPS stock solution and mixed with an equal volume of fetal bovine serum (Invitrogen) to reach a final dye concentration of 2 mM (Vranesic et al., 1994). After incubation, the slices were rinsed with Krebs' solution to wash out the dye that was not incorporated by the tissue, before being transferred to the recording chamber installed on an upright epifluorescence microscope (SliceScope, Scientifica), equipped with a 20× objective (XLUMPlanFl, 0.95 numerical aperture, water-immersion; Olympus). The light generated by a halogen lamp (10 V, 150 W; model LM150, MORITEX) was controlled by an electronic shutter (Newport), and then passed through an excitation filter (λ = 535 ± 20 nm), projected onto a dichroic mirror (λ = 565 nm), and reflected toward the objective lens to illuminate the specimen. Fluorescence generated by the tissue was transmitted through an absorption filter (λ > 580 nm) to the CCD camera (MICAM01, SciMedia/Brain Vision). The whole imaging system was connected through an input/output interface (Brain Vision) to a PC controlling illumination, stimulation, and data acquisition. The final pixel size was 4.5 × 4.5 μm with a 20× objective. Full-frame image acquisition was performed at 0.5 kHz. Data were acquired and displayed using Brain Vision software, and signals were analyzed using custom-made routines written in MATLAB (MathWorks). At the beginning of recordings, a calibration procedure was adopted to ensure homogeneity across experiments. The dynamic range of the CCD camera was calibrated by measuring background fluorescence and setting the average light intensity in the absence of stimulation to 50% of the saturation level. The background fluorescence was sampled for 50 ms before triggering electrical stimulation and was used to measure the initial fluorescence intensity (F_0). The relative fluorescence change ($\Delta F/F_0$) was then calculated for each time frame. The signal-to-noise ratio was improved by averaging 10 consecutive sweeps at the stimulus repetition frequency of 0.1 Hz.

VSDi data analysis. Fluorescence data collected by Brain Vision acquisition software were filtered using both a cubic filter (3 × 3) and a spatial filter (3 × 3) embedded in the software, and then were exported and processed in MATLAB. The resulting files were a series of matrices each representing a temporal frame of the acquired trace. Using appropriate MATLAB routines written ad hoc, single matrices representing the peak value of granular layer responses to electrical stimulation were obtained. These maps containing the information on the signal peak amplitudes and their spatial origin were used for comparison of control condition and different treatments, as detailed below. Data were reported as the mean ± SEM. Statistical significance was assessed using unpaired Student's t test unless otherwise stated. For the analysis of the amount and spatial distribution of the NMDA receptor component of excitation in the cerebellar granular layer of WT and IB2 KO mice, responses to electrical stimulation of the mossy fibers were recorded in control and after perfusion of the NMDA receptor blocker APV (50 μM). The average map of APV effect on signal amplitudes was subtracted from the control map to unveil the contribution of the NMDA receptors. The spatial distribution of the NMDA receptor-mediated depolarization was revealed by averaging each experimental map on the peak of NMDA receptor component in each case. Whenever spatial maps obtained from different experiments were averaged, the corresponding slices were aligned along the mossy fiber bundle. For the analysis of the E/I balance and spatial distribution of excitation and inhibition in the granular layer, similar experiments were performed, recording the responses to medium frequency stimulation before and after the perfusion of the $GABA_A$ receptor

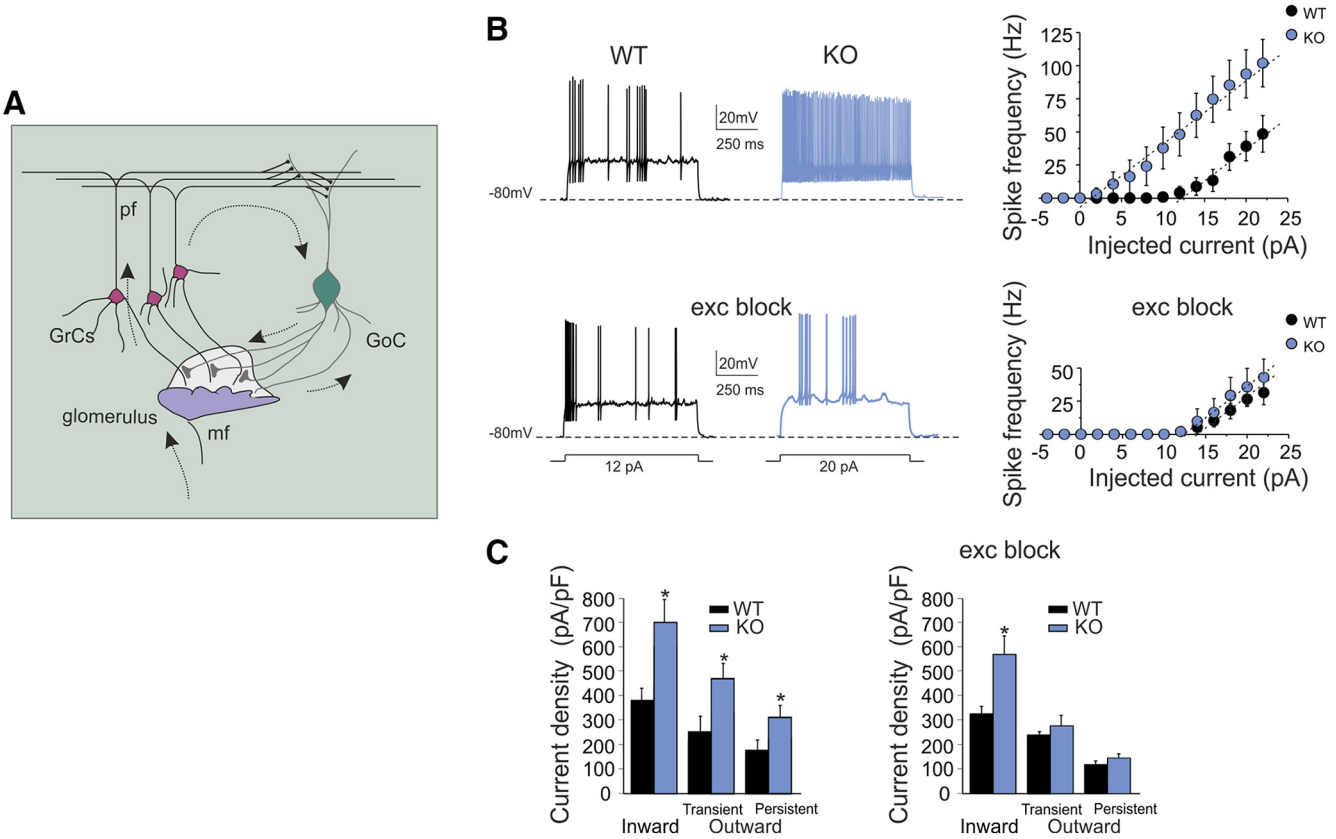

Figure 1. Granule cell excitable properties. ***A***, Schematic representation of cerebellar circuit. Mossy fibers (mf) contact granule cell (GrC) and Golgi cell (GoC) dendrites. Axons of GrCs, the parallel fibers (pf), activate Golgi cells that inhibit GrCs through feedforward and feedback inhibitory loops. ***B***, Granule cell electroresponsiveness in presence of 10 μM gabazine (control condition) and glutamate receptor antagonists (10 μM NBQX, 50 μM D-APV, and 50 μM 7-Cl-Kyn acid). Voltage responses were elicited from −80 mV using step current injection. The plots show the relationships between average spike frequency over 800 ms and the injected current intensity both for WT and IB2 KO granule cells. Data are reported as the mean ± SEM. Linear fits in control condition were as follows (dashed lines): WT: *x*-intercept, 11.7 ± 0.8 pA; slope, 5.7 ± 0.9 spike/pA ($n = 6$); IB2 KO: *x*-intercept, 5.5 ± 2.5 pA ($p = 0.04$); slope, 6.5 ± 0.5 spike/pA ($n = 8$; $p = 0.46$). Data are reported as the mean ± SEM. Linear fits in the presence of glutamate receptor antagonists were as follows (dashed lines): WT: *x*-intercept, 11.0 ± 1.6 pA; slope, 3.6 ± 0.4 spike/pA ($n = 8$); IB2 KO: *x*-intercept, 13.1 ± 1.8 pA ($p = 0.4$); slope 5.6 ± 1.15 spike/pA ($n = 6$; $p = 0.15$). ***C***, Voltage-activated inward and outward currents in granule cells. The histograms compare inward and outward current densities (normalized by input C_m) measured at −40 and +20 mV in WT and IB2 KO mice in the presence of 10 μM gabazine (control condition) and glutamate receptor antagonists (10 μM NBQX, 50 μM D-APV, and 50 μM 7-Cl-Kyn acid). Data are reported as the mean ± SEM. *$p < 0.05$.

antagonist SR95531 (gabazine; 10 μM). This approach allows reconstruction of a map of regions with prevailing E compared with regions showing prevailing I (Mapelli and D'Angelo, 2007; Gandolfi et al., 2014). In this case, the E map was constructed on the control responses (where the response is available only in the regions where excitation prevails over inhibition), while the I map was constructed subtracting the maps after SR95531 perfusion to the control maps (unveiling the regions where, before SR95531 perfusion, excitation was prevented by inhibition). Both E and I maps were normalized to 1, and the E/I balance maps were obtained as (E − I)/E. The C/S organization of E and I was evident by averaging the E/I maps in each experiment on the peak of excitation in controls. For the analysis of the amount and spatial distribution of LTP and long-term depression (LTD) in the granular layer, plasticity maps were obtained by comparing response amplitudes before and after the plasticity induction through an HFS delivered to the mossy fiber bundle. The C/S spatial organization of LTP and LTD was unveiled by averaging each plasticity map from different experiments on the peak of the maximum LTP.

Statistical analysis. Results are reported as the mean ± SEM and compared for their statistical significance by unpaired Student's test (unless otherwise stated; a difference was considered significant at $p < 0.05$).

Results

In the cerebellum granular layer, there are three main mechanisms controlling the E/I balance of granule cells (Nieus et al., 2014), as follows: granule cell intrinsic excitability, mossy fiber glutamatergic excitation, and Golgi cell GABAergic inhibition (Mapelli et al., 2014; Fig. 1*A*). Here, these properties have been compared in turn between IB2 KO and WT mice. In patch-clamp whole-cell recordings in acute cerebellar slices, there were no significant differences in resting membrane potential between IB2 KO and WT cerebellar granule cells, but there was a small but significant difference in passive membrane properties (see below and Table 1).

Enhanced intrinsic excitability in IB2 KO granule cells

In whole-cell current-clamp recordings, both WT and IB2 KO granule cells were silent at rest and responded to current steps with fast repetitive spike discharges that increased their frequency almost linearly with stimulus intensity (D'Angelo et al., 1995, 1998; Brickley et al., 1996; Rossi et al., 1998; Armano et al., 2000; Cathala et al., 2003; Prestori et al., 2008; Fig. 1*B*). However, IB2 KO granule cells showed a higher discharge frequency compared with WT granule cells both at low current injection [12 pA: WT = 4.1 ± 0.1 Hz ($n = 6$); IB2 KO = 48.1 ± 14.2 Hz ($n = 8$); $p = 0.017$, unpaired *t* test] and at high current injection [20 pA: WT = 39.2 ± 9.5 Hz ($n = 6$); IB2 KO = 93.7 ± 16.0 Hz ($n = 8$); $p = 0.014$, unpaired *t* test], shifting the frequency–intensity plot toward the left (Fig. 1*B*). In the same experiments, whole-cell currents elicited by depolarizing voltage steps differed in WT and

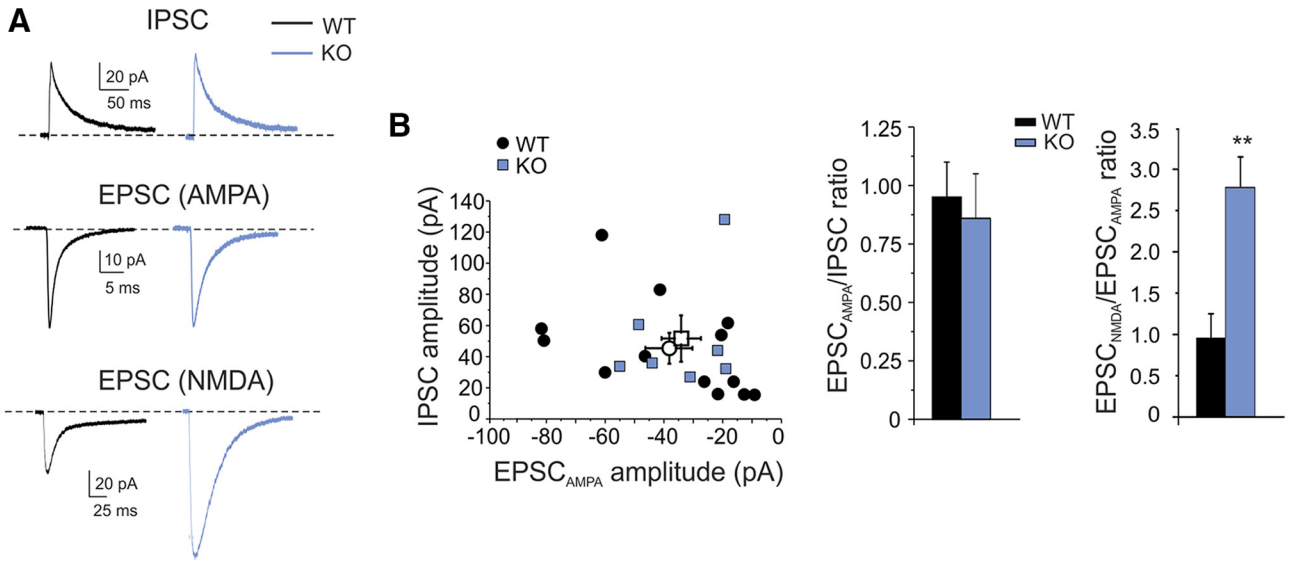

Figure 2. Evoked excitatory and inhibitory currents in granule cells. ***A***, Synaptic currents in WT and IB2 KO granule cells. The $EPSC_{AMPA}$ and IPSC values are recorded from the same cells at the holding potential of −70 mV (average of 30 consecutive traces) and at +10 mV (average of 10 consecutive traces), respectively. The $EPSC_{NMDA}$ values are recorded in different cells at −70 mV in Mg^{2+}-free extracellular solution in the presence of the AMPA receptor antagonist 10 μM NBQX (average of 30 consecutive traces). ***B***, IPSC/EPSC ratios at mossy fiber–granule cell synapses in WT and IB2 KO mice. The plot shows the amplitude of $EPSC_{AMPA}$ and IPSC in the same cells for WT and IB2 KO mice (open symbols, mean ± SEM). The histogram compares the average $EPSC_{AMPA}$/IPSC ratio and $EPSC_{NMDA}$/IPSC ratio in WT and IB2 KO mice. Data are reported as the mean ± SEM. $^{**}p < 0.01$.

IB2 KO granule cells (Fig. 1*C*). The transient inward current density (corresponding to a fast Na^+ current; Magistretti et al., 2006) was significantly larger in IB2 KO compared with WT granule cells. The transient and persistent outward current densities (comprising A-type, delayed rectifier, and calcium-dependent K^+ currents; Bardoni and Belluzzi, 1994) were also significantly larger in IB2 KO compared with WT granule cells. It should be noted that input C_m was slightly but significantly smaller and that input R_m was slightly but significantly higher in IB2 KO compared with WT granule cells (Table 1). Therefore, differences in both current density changes and passive membrane properties support the concept that IB2 KO granule cells were more excitable than WT granule cells.

To investigate whether tonic currents or background synaptic activity (Mitchell and Silver, 2000, 2003; Rossi et al., 2002) could influence the frequency–intensity plots, experiments have also been performed in the presence of excitatory receptor blockers (Fig. 1*B*). In WT granule cells, the perfusion of AMPA and NMDA receptor antagonists did not cause any significant changes in the frequency–intensity plot, which showed a similar discharge frequency compared with control both at low current injection [12 pA: 5.3 ± 3.0 Hz ($n = 8$) vs 4.1 ± 0.1 Hz ($n = 6$); $p = 0.76$, unpaired t test] and at high current injection [20 pA: = 26.6 ± 5.6 Hz ($n = 8$) vs 39.2 ± 9.5 Hz ($n = 6$); $p = 0.28$, unpaired t test; Fig. 1*B*]. Interestingly, in IB2 KO granule cells, the perfusion of AMPA and NMDA receptor antagonists caused a significant reduction in excitability, so that the frequency–intensity plot did no longer differ from that of WT granule cells. The discharge frequency was similar both at low current injection [12 pA: WT = 5.3 ± 3.0 Hz ($n = 8$); IB2 KO = 2.0 ± 1.5 Hz ($n = 6$); $p = 0.34$, unpaired t test] and at high current injection [20 pA: WT = 26.6 ± 5.6 Hz ($n = 8$); IB2 KO = 35.7 ± 12.0 Hz ($n = 6$); $p = 0.52$, unpaired t test; Fig. 1*B*]. Moreover, in IB2 KO granule cells, in the presence of glutamate receptor antagonists, the outward current densities were not different from WT granule cells (Fig. 1*C*). These data suggest that, in IB2 KO mice, the increased granule cell responsiveness could be related to excitatory receptor activation by tonic glutamate and consequent deregulation of membrane ionic currents (Sah et al., 1989; Nieus et al., 2006; Le Meur et al., 2007).

Similar AMPA and $GABA_A$ but increased NMDA receptor-mediated currents at IB2 KO granule cell synapses

Mossy fiber stimulation is known to elicit EPSCs directly through mossy fiber activation, and IPSCs indirectly through activation of Golgi cells (Fig. 1*A*; Cathala et al., 2003; Cesana et al., 2013; Nieus et al., 2014). Postsynaptic currents were recorded from granule cells both at −70 and +10 mV to isolate the excitatory (EPSC) from the inhibitory (IPSC) component. This technique was reported previously (Mapelli et al., 2009; Nieus et al., 2014). It should be noted that, at −70 mV, NMDA receptor-mediated currents are blocked by Mg^{2+}, so that the EPSC is almost purely AMPA receptor mediated. In the present experiments, the AMPA-EPSC peak [WT = −38.1 ± 7.1 pA ($n = 13$) vs IB2 KO = −34.1 ± 5.7 ($n = 7$); $p = 0.66$] and the $GABA_A$-IPSC peak [WT = 45.4 ± 8.4 pA ($n = 13$) vs IB2 KO = 51.7 ± 13.4 ($n = 7$); $p = 0.69$] showed similar amplitudes in WT and IB2 KO mice (Fig. 2*A*). Accordingly, no differences were observed in the AMPA-EPSC/$GABA_A$-IPSC ratio in granule cells [WT = 0.95 ± 0.15 ($n = 13$) vs IB2 KO = 0.86 ± 0.19 ($n = 7$); $p = 0.71$; Fig. 2*B*].

In a different series of recordings, the NMDA EPSC was elicited in isolation at −70 mV in a Mg^{2+}-free solution in the presence of AMPA and $GABA_A$ receptor blockers (10 μM NBQX and 10 μM SR95531, respectively; Fig. 2*A*). The NMDA-EPSC peak was enhanced in IB2 KO synapses [WT = −37.0 ± 5.1 pA ($n = 6$) vs IB2 KO = −95.3 ± 17.7 ($n = 5$); $p = 0.03$] by 2.5 times. These results confirm the alteration in NMDA EPSC amplitude reported previously (Giza et al., 2010).

In aggregate, the similarity of the AMPA-EPSC and $GABA_A$-IPSC, along with the large increase of the NMDA-EPSC, suggest that the E/I balance in IB2 KO mice will move in favor of excitation in conditions in which the NMDA channels are physiologically unblocked by depolarization.

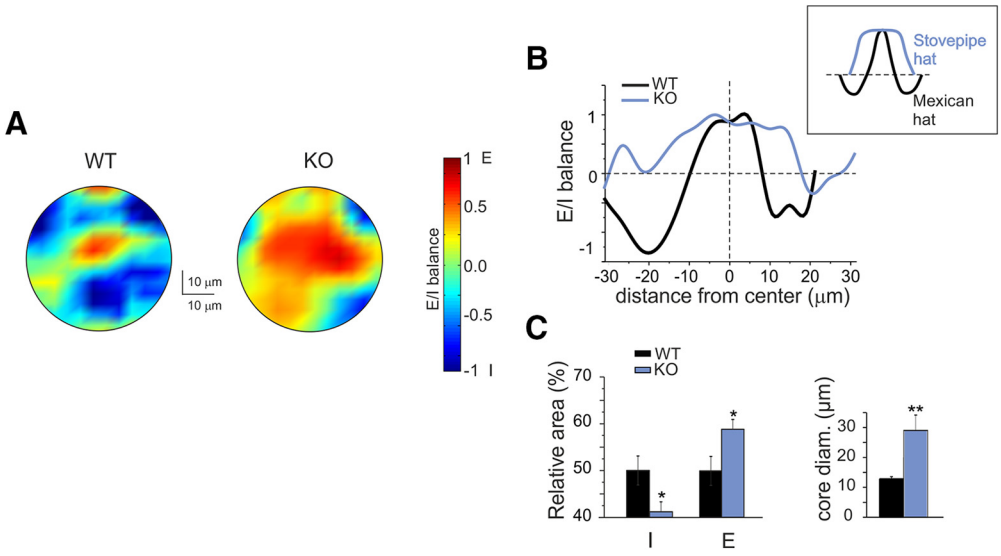

Figure 3. Excitatory/inhibitory balance and center/surround organization in the granular layer. ***A***, VSDi normalized maps showing the spatial distribution of excitation and inhibition in WT and IB2 KO granular layers (average of 5 recordings in both cases). ***B***, The plot shows the E/I balance as a function of distance from the center for the maps shown in ***A***. Note that in the IB2 KO granular layer the excitation core is broader, while the inhibited surround is reduced, compared with the WT granular layer. This tends to change the C/S from the typical Mexican hat shape in controls to the stovepipe hat shape in IB2 KO mice (inset). ***C***, The histograms show, in WT and IB2 KO mice, the average values of the inhibition or excitation areas and of the core diameter. Data are reported as the mean ± SEM. $*p < 0.05$, $**p < 0.01$.

Increased excitation in C/S structures of IB2 KO granular layer is driven by NMDA currents

To obtain a physiological assessment of the E/I balance and of the NMDA current contribution, we used VSDi. VSDi allows the generation of maps of electrical activity and the investigation of the spatial distribution of granular layer responses following mossy fiber stimulation (Mapelli et al., 2010). In particular, VSDi, coupled with selective pharmacological blockade of synaptic receptors, can reveal the relative roles of synaptic inhibition and NMDA receptors (Gandolfi et al., 2015).

A first set of VSDi recordings was performed by subtracting control activity maps from those obtained after $GABA_A$ receptor blockade with 10 μM SR95531 (Fig. 3; for details, see Materials and Methods). In agreement with previous observations, the granular layer response to mossy fiber stimuli self-organized in C/S structures characterized by a Mexican hat profile, with an excitation core surrounded by inhibition (Mapelli and D'Angelo, 2007; Solinas et al., 2010; Gandolfi et al., 2014, 2015; Fig. 3*A*,*B*). The C/S distribution was maintained in the IB2 KO granular layer but with striking differences. (1) Excitation was enhanced generating larger cores compared with WT (core diameter: WT = 12.9 ± 1.7 μm vs IB2 KO = 29.5 ± 4.9 μm; $n = 5$ for both; $p = 0.0106$; Fig. 3*C*). (2) Inhibition was weaker in the surround (WT/KO ratio = 2.83 ± 0.17, $n = 5$). (3) Granular layer areas showing excitation were consequently larger in IB2 KO mice than in WT mice (WT = 49.9 ± 3.1% vs IB2 KO = 58.8 ± 2.1%; $n = 5$ for both; $p = 0.0468$; Fig. 3*C*). As a result, the altered C/S organization in IB2 KO mice showed larger excitation cores with poor inhibitory surrounds, shifting from the Mexican hat shape to the so-called stovepipe hat shape (Fig. 3*B*).

A second set of VSDi recordings was performed by subtracting control activity maps from those obtained after NMDA receptor blockade with 50 μM APV (Fig. 4; for details, see Materials and Methods). As expected from the increased NMDA receptor-mediated current reported in Figure 2, the NMDA receptor-mediated component of the VSDi signal was larger in IB2 KO than WT granular layers (ratio KO/WT = 2.16 ± 0.29; $n = 5$ for both). The maps showing the spatial organization of the NMDA receptor contribution to the excitatory response were similar to the C/S organization shown in Figure 3, with peaks of NMDA receptor contribution in cores with a diameter of 26.1 ± 1.7 μm in IB2 KO versus 18.9 ± 1.6 μm in WT ($n = 5$ for both; $p = 0.015$; Fig. 4*A*,*B*). Interestingly, since during VSDi membrane potential remains unclamped, allowing voltage-dependent NMDA channel unblock during depolarization, these maps provide information about the nonlinear contribution of NMDA currents. This result supported the hypothesis that the enhanced NMDA receptor-mediated transmission revealed in Figure 2 was indeed a key player in determining the C/S and E/I alterations in the IB2 KO granular layer.

Enhanced long-term potentiation at the IB2 KO mossy fiber–granule cell relay

Mossy fiber–granule cell LTP is NMDA receptor dependent through the synaptic control of postsynaptic intracellular calcium elevation (D'Angelo et al., 1999; Maffei et al., 2003; Gall et al., 2005; D'Errico et al., 2009). The impact of elevated NMDA receptor-dependent neurotransmission on LTP induction in IB2 KO mice was evaluated using a continuous HFS train (Fig. 5*A*) delivered from the holding potential of −50 mV in current clamp (Gall et al., 2005; D'Errico et al., 2009). During HFS, IB2 KO generated more spikes than WT granule cells [WT = 23.5 ± 5.3 ($n = 12$) vs IB2 KO = 54.2 ± 11.4 ($n = 9$); $p = 0.015$; Fig. 5*A*,*B*], which is in line with the enhancement in NMDA currents (D'Angelo et al., 2005) and in intrinsic firing reported above (Figs. 1, 2). After HFS, the changes were evaluated over at least 25 min after HFS.

The AMPA EPSC increased both in WT and IB2 KO mice and remained potentiated throughout the recordings (Fig. 5*C*). The increase in amplitude of AMPA-EPSCs was approximately fivefold larger in IB2 KO mice than in WT mice [WT = 20.4 ± 4.2% ($n = 12$) vs IB2 KO = 102.4 ± 34.9% ($n = 9$); $p = 0.047$; Fig. 5*D*].

Intrinsic excitability increased more in WT mice than in IB2 KO mice (Fig. 6*A*,*B*). The current needed to generate spikes (cur-

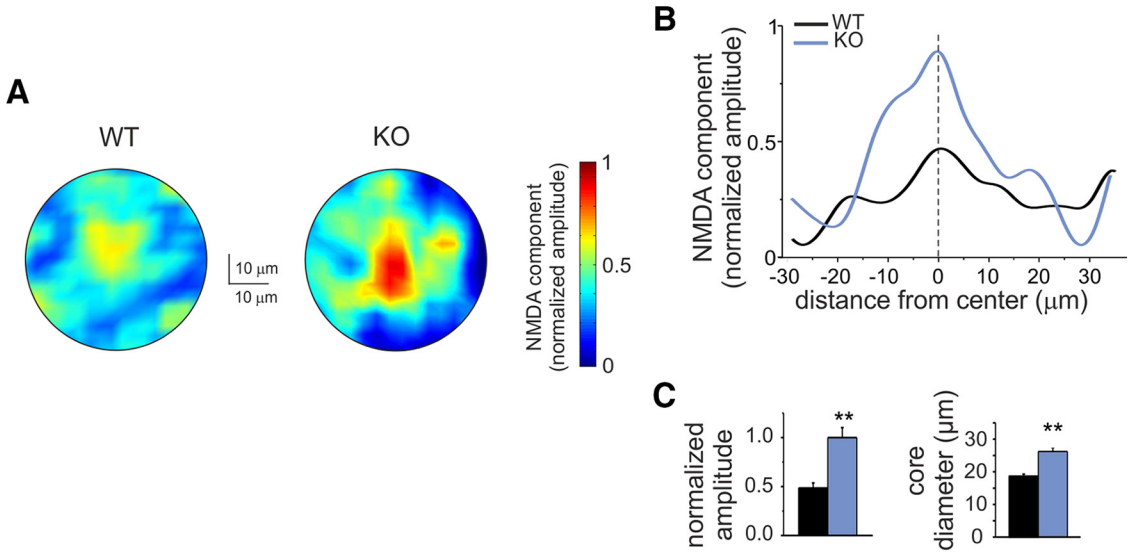

Figure 4. NMDA receptor-dependent component of granular layer excitation. ***A***, VSDi normalized maps showing the spatial distribution of the NMDA component of excitation in WT and IB2 KO granular layers (average of 5 recordings in both cases). ***B***, The plot shows the NMDA component as a function of distance from the center for the maps shown in ***A***. Note that in the IB2 KO granular layer the NMDA component of excitation is larger and more extended compared with the WT granular layer. ***C***, The histograms show, in WT and IB2 KO mice, the average values of the NMDA component normalized amplitude and of the core diameter. Data are reported as the mean ± SEM. $^{**}p < 0.01$.

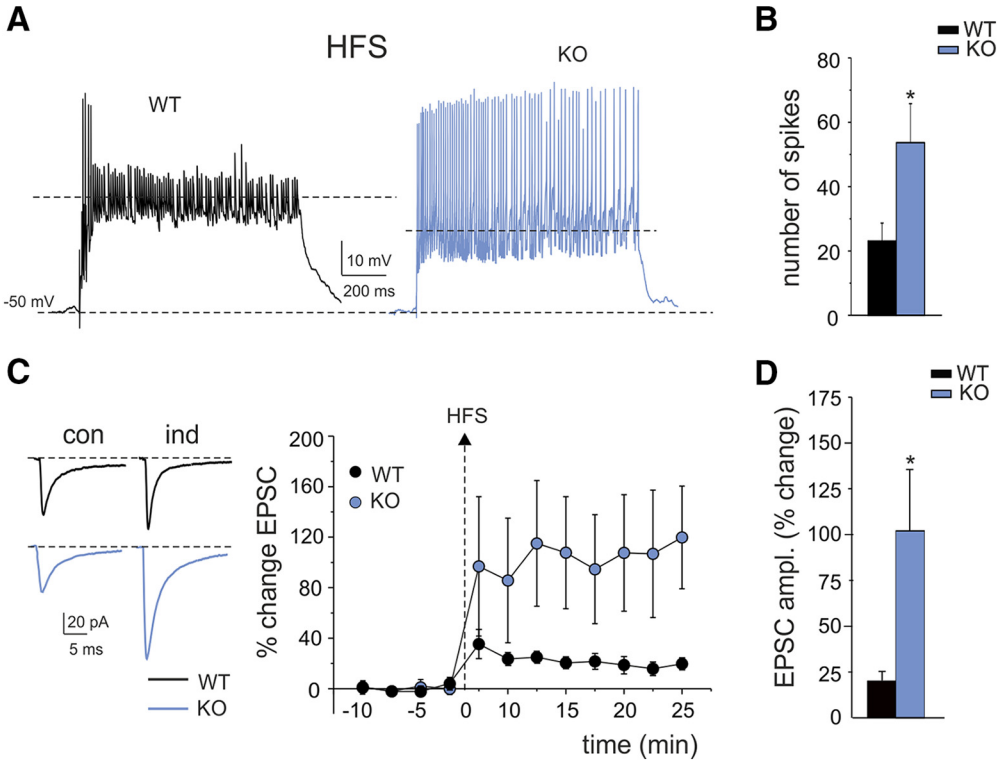

Figure 5. LTP of mossy fiber–granule cell EPSCs. ***A***, Granule cell synaptic responsiveness. Voltage responses were elicited from −50 mV during 1 s, 100 Hz synaptic stimulation (HFS) used for plasticity induction. Note the stronger spike generation in IB2 KO than in WT mice. ***B***, The histogram shows the average number of spikes during HFS in WT and IB2 KO mice. Data are reported as the mean ± SEM. $^{*}p < 0.05$. ***C***, Long-lasting effects of HFS on $EPSC_{AMPA}$ in WT and IB2 KO granule cells. $EPSC_{AMPA}$ (average of 30 tracings in both cases) are recorded in controls and 20 min after HFS. Note that, after HFS stimulation, the $EPSC_{AMPA}$ increase was larger in IB2 KO than WT mice. The LTP plot shows the average time course of $EPSC_{AMPA}$ amplitude changes in WT granule cells ($n = 12$) and IB2 KO granule cells ($n = 9$). Data are reported as the mean ± SEM. $^{*}p < 0.05$. ***D***, The histogram shows the average $EPSC_{AMPA}$ LTP following HFS in WT and IB2 KO mice. Data are reported as the mean ± SEM. $^{*}p < 0.05$.

rent threshold) decreased significantly compared with control in WT granule cells (−42.8 ± 7.7%; $n = 6$; $p = 0.0055$) but not in IB2 KO granule cells (−8.6 ± 14.4%; $n = 8$; $p = 0.07$; Fig. 6*B*). Moreover, the increase in spike frequency was less pronounced in IB2 KO than in WT granule cells [WT = 102.6 ± 19.3% ($n = 6$) vs IB2 KO = 21.1 ± 8.7% ($n = 8$); $p = 0.032$; Fig. 6*B*]. A possible explanation of this effect could be that granule cell intrinsic excitability was already increased in IB2 KO granule cells (compare Fig. 1*B*), such that the level of IB2 KO granule cell excitability in control was similar to that in WT granule cells after potentiation (Fig. 6*B*).

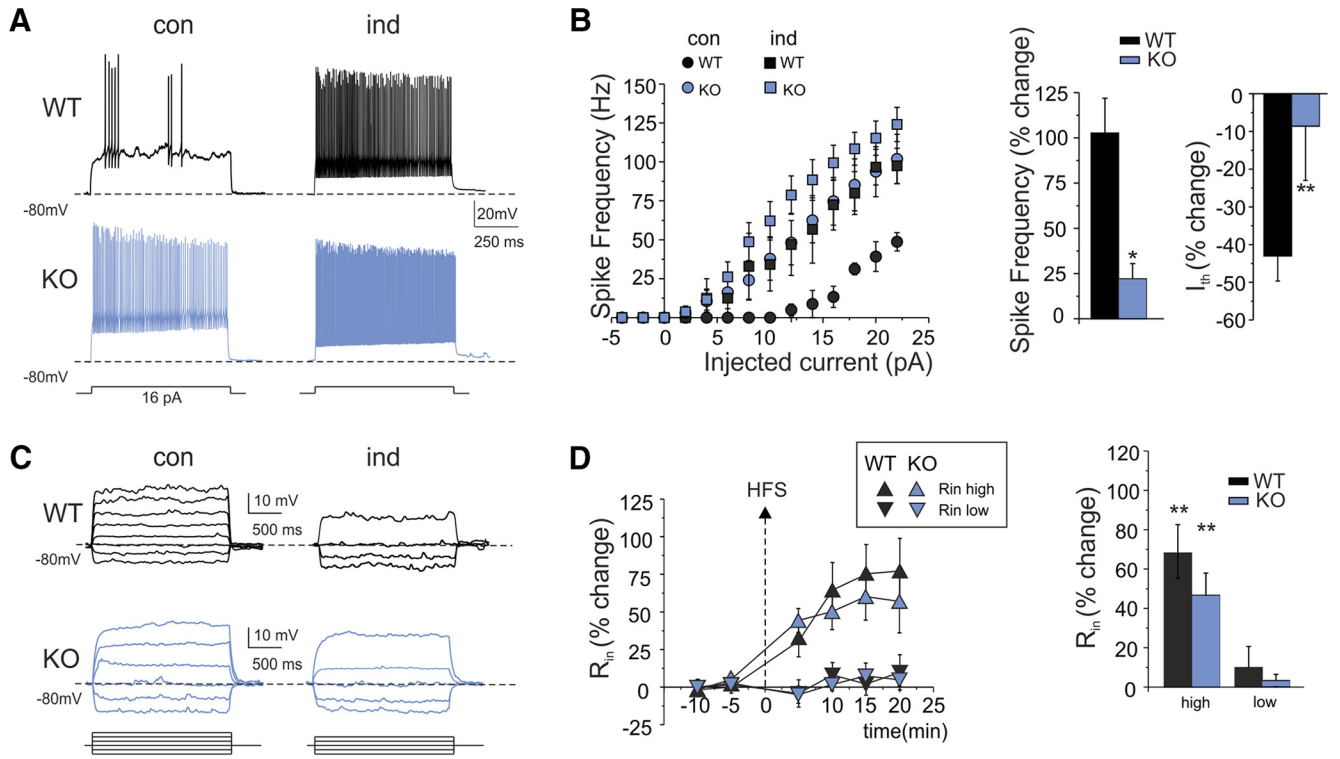

Figure 6. Long-term enhancement in granule cells intrinsic excitability. ***A***, Voltage responses to current injection in WT and IB2 KO granule cells recorded in control and 20 min after HFS. Note that HFS enhances spike generation both in WT and IB2 KO granule cells. ***B***, Spike frequency is plotted as a function of current injection in control conditions and after HFS both in WT and in IB2 KO mice. Note that, after HFS, spike frequency increases more in WT than in IB2 KO mice. The histograms compare the average spike frequency and threshold current (I_{th}) changes in WT and IB2 KO mice. Data are reported as the mean ± SEM. $^{*}p < 0.05$, $^{**}p < 0.01$. ***C***, Subthreshold voltage responses to current injection in WT and IB2 KO granule cells recorded in controls and 20 min after HFS. Note that the voltage response in the high-potential region is enhanced both in WT and IB2 KO granule cells. ***D***, The plot shows the average time course of R_{in} changes after HFS stimulation in two subthreshold membrane potential regions, less than −70 mV ($R_{in\text{-}low}$) and more than −70 mV ($R_{in\text{-}high}$). After HFS, in both WT and IB2 KO granule cells, $R_{in\text{-}high}$, but not $R_{in\text{-}low}$, increased. The histogram shows the average R_{in} changes for WT and IB2 KO mice. Data are reported as the mean ± SEM. $^{**}p < 0.01$.

As a further control, we monitored the apparent granule cell input resistance (Fig. 6*C*,*D*) by measuring the response to small current steps (causing ~10 mV potential changes) either below −70 mV ($R_{in\text{-}low}$) or above −70 mV ($R_{in\text{-}high}$; Armano et al., 2000). After HFS, $R_{in\text{-}high}$ rapidly increased in both WT and IB2 KO mice following a similar time course, and remained potentiated throughout the recordings (at least 20 min after HFS; Fig. 6*D*, average time courses). At 20 min after HFS, the $R_{in\text{-}high}$ increase was 67.8 ± 16.5% ($n = 8$; $p = 0.0014$) in WT mice and 46.9 ± 9.0% ($n = 10$) in IB2 KO mice ($p = 0.00012$). This change was likely to contribute to the increased intrinsic excitability in both WT and IB2 KO mice. It should be noted that $R_{in\text{-}low}$ values remained unchanged in both WT and IB2 KO mice, providing an internal control for recording stability (Fig. 6*C*,*D*).

LTP dependence on NMDA and $GABA_A$ receptors in IB2 KO granule cells

The role of NMDA receptors in the induction of long-term potentiation between mossy fiber–granule cell synapses is well established (D'Angelo et al., 1999, 2005; Armano et al., 2000; Maffei et al., 2002; Sola et al., 2004; D'Errico et al., 2009). To test whether LTP in these experiments was NMDA receptor dependent, we first evaluated whether HFS could induce LTP when NMDA receptors were blocked. When the NMDA receptors antagonists D-APV (50 μM) and 7-Cl-Kyn acid (50 μM) were added to the extracellular solution, HFS failed to induce LTP in both WT and IB2 KO mice (WT: 0.23 ± 5.9%; $n = 7$; $p = 0.89$; vs IB2 KO: −22.9 ± 4.9%; $n = 6$; $p = 0.03$; Fig. 7*A*). Interestingly, a significant LTD appeared in IB2 KO mice.

NMDA receptor-dependent LTP in the granular layer strongly depends on depolarization during the induction and activation of $GABA_A$ receptors, which, by limiting depolarization, can indeed prevent LTP (Armano et al., 2000; Maffei et al., 2002). To test whether LTP in these experiments could be prevented by $GABA_A$ receptors, in a set of experiments the $GABA_A$ receptors antagonist gabazine was omitted from the extracellular solution. Figure 7*B* shows the time course of EPSC changes. The removal of gabazine prevented LTP in both WT mice and IB2 KO mice (WT: −12.6 ± 8.6%; $n = 7$; $p = 0.38$; vs IB2 KO: −36.4 ± 8.3%; $n = 7$; $p = 0.005$). Interestingly, a significant LTD appeared in IB2 KO mice.

These results indicate that in IB2 KO mice as in WT mice, LTP induction requires NMDA receptor activation and can be prevented by $GABA_A$ receptor activation. However, in IB2 KO mice, NMDA and $GABA_A$ receptor blockers unveiled an underlying LTD.

Different mechanisms of LTP expression

LTP expression was first assessed by analyzing changes in EPSC amplitude, variability (CV), and PPR (Fig. 8*A*). The PPR of EPSCs is generally considered to reflect changes in the probability of transmitter release in a pair of stimuli (Zucker and Regehr, 2002), while the CV of EPSCs is a readout of presynaptic variability of quantal transmitter release upon repeated stimulation nor-

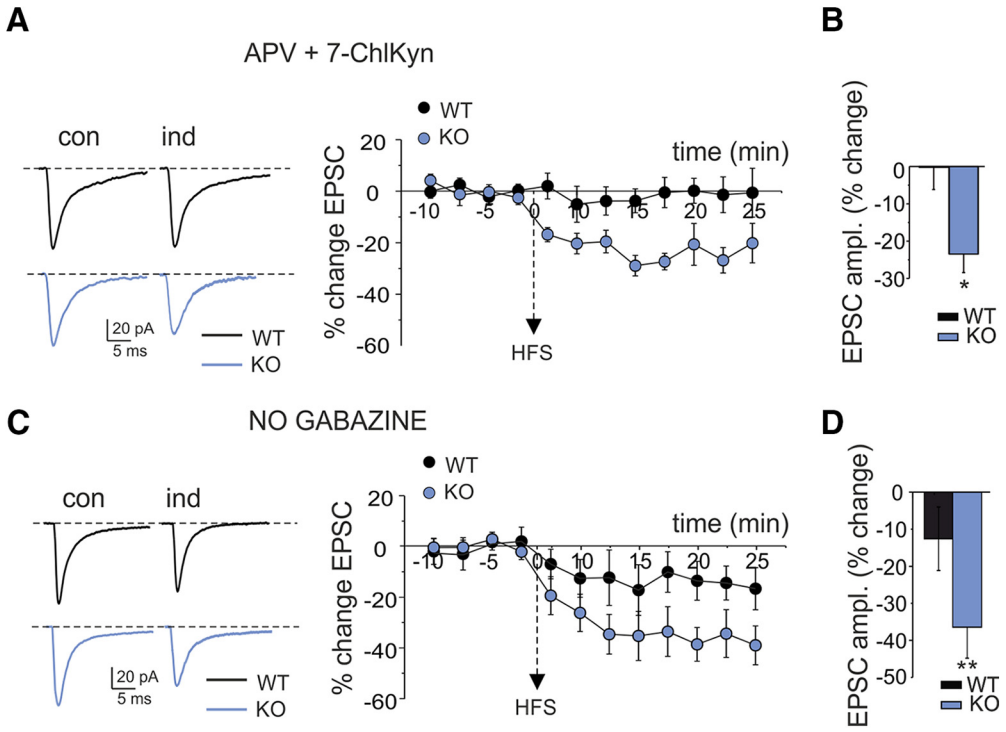

Figure 7. NMDA and $GABA_A$ receptor dependence of LTP. ***A***, Long-lasting effects of HFS on $EPSC_{AMPA}$ in WT and IB2 KO granule cells during the blockade of NMDA receptors with D-APV (50 μM) and 7-Cl-Kyn acid (50 μM). $EPSC_{AMPA}$ (average of 30 tracings in both cases) are recorded in controls and 20 min after HFS. Note that, after HFS stimulation, IB2 KO cells show LTD, while WT cells do not show any significant changes. The plot shows the average time course of $EPSC_{AMPA}$ amplitude changes in WT ($n = 7$) and IB2 KO ($n = 6$) granule cells. Data are reported as the mean ± SEM. ***B***, The histogram shows the average $EPSC_{AMPA}$ change following HFS in WT and IB2 KO mice. Data are reported as the mean ± SEM. *$p < 0.05$. ***C***, Long-lasting effects of HFS on $EPSC_{AMPA}$ in WT and IB2 KO granule cells in a gabazine-free extracellular solution. $EPSC_{AMPA}$ values (average of 30 tracings in both cases) are recorded in controls and 20 min after HFS. Note that, after HFS stimulation, the LTP observed in controls is no longer visible and is substituted for by an $EPSC_{AMPA}$ LTD in IB2 KO mice that is larger than that in WT mice. The plot shows the average time course of $EPSC_{AMPA}$ amplitude changes in WT ($n = 6$) and IB2 KO ($n = 7$) granule cells. Data are reported as mean ± SEM. ***D***, The histogram shows the average $EPSC_{AMPA}$ change following HFS in WT and IB2 KO mice. Data are reported as mean ± SEM. **$p < 0.01$.

malized by the mean (Malinow and Tsien, 1990; Manabe et al., 1993). In the recordings used for PPR and CV analysis, after HFS, the EPSCs showed a significant increase in WT mice (18.2 ± 3.4; $n = 8$; $p = 0.012$) and IB2 KO mice (106.8 ± 51.8%; $n = 5$; $p = 0.05$), while PPR (interstimulus interval, 20 ms) showed a significant reduction in WT (−19.6 ± 9.3%; $n = 8$; $p = 0.033$) but not in IB2 KO (−6.7 ± 3.3%; $n = 5$; $p = 0.1$). Interestingly, CV significantly decreased in both WT and IB2 KO (WT: −28.3 ± 6.7; $n = 12$; $p = 0.002$; IB2 KO: −30.0 ± 8.0; $n = 9$; $p = 0.012$). The CV decrease suggested that neurotransmitter release was increased not just in WT (Sola et al., 2004), but also in IB2 KO mice, although with some differences (see below).

The CV and PPR analysis cannot stand alone in determining the changes that could affect the neurotransmission process (Yang and Calakos, 2013). A further way to assess whether EPSC changes depend on the number of releasing sites, release probability, or quantum size is to plot $(CV_2/CV_1)^{-2}$ versus (M_2/M_1) (Bekkers and Stevens, 1990; Malinow and Tsien, 1990; Fig. 8*B*). The WT experimental data points were distributed homogeneously in the quadrant corresponding to *p*/*n* increase, with no point falling in the regions of a pure *n* or *q* change. Conversely, the IB2 KO experimental dataset was heterogeneously distributed over regions of *p*, *n*, or *q* increase. These data distributions suggested that multiple presynaptic and postsynaptic mechanisms contributed to determine LTP at IB2 KO mossy fiber–granule cell synapses.

A second experimental approach to quantal analysis is to examine mEPSCs before and after LTP induction (Fig. 8*C*,*D*; Kullmann and Nicoll, 1992; Wyllie et al., 1994; Malgaroli et al., 1995). This method is especially useful at multiquantal release synapses, as previously described (Sola et al., 2004; Saviane and Silver, 2006), and can allow the difference between an increase in quantum content (*p* or *n*) or *q* to be distinguished. Since here mEPSCs accounted for the whole spontaneous mossy fiber activity, in LTP experiments mEPSCs were recorded without TTX and were used to characterize the LTP expression mechanism (Sola et al., 2004). Moreover, to prevent mEPSC changes from being obscured by the contribution of nonpotentiated synapses, we activated as many synapses as possible by raising stimulus intensity. Indeed, in these recordings, the EPSCs [−59.0 ± 11.0 pA ($n = 4$) in WT mice and −55.0 ± 14.9 pA ($n = 4$) in IB2 KO mice] were about twice as large than those measured in Figure 2 (by comparison with single-fiber EPSCs measured in similar recording conditions, this corresponded to activation of two to three mossy fibers; Sola et al., 2004). After HFS, the EPSCs increased (WT: 19.0 ± 2.0%; $n = 4$; $p = 0.02$; vs IB2 KO: 93.6 ± 49.7; $n = 4$; $p = 0.02$), confirming larger LTP induction in IB2 KO mice than WT mice (compare Fig. 8*A*). In the same recordings, the amplitudes of mEPSCs did not vary in WT granule cells (3.3 ± 3.7%; $n = 4$; $p = 0.4$) but showed a significant increase in IB2 KO granule cells (28.9 ± 5.66%; $n = 4$; $p = 0.016$). Conversely, mEPSC frequency showed a significant increase in WT granule cells (46.1 ± 12.9%; $n = 4$; $p = 0.016$) but did not show any significant changes in IB2 KO granule cells (−16.9 ± 6.0%; $n = 4$; $p = 0.11$). Therefore, mEPSC analysis indicated that, while WT granule cells showed an increase in quantum content (as reported previously in rats (Sola et al., 2004), IB2 KO granule cells showed an increased quantum size.

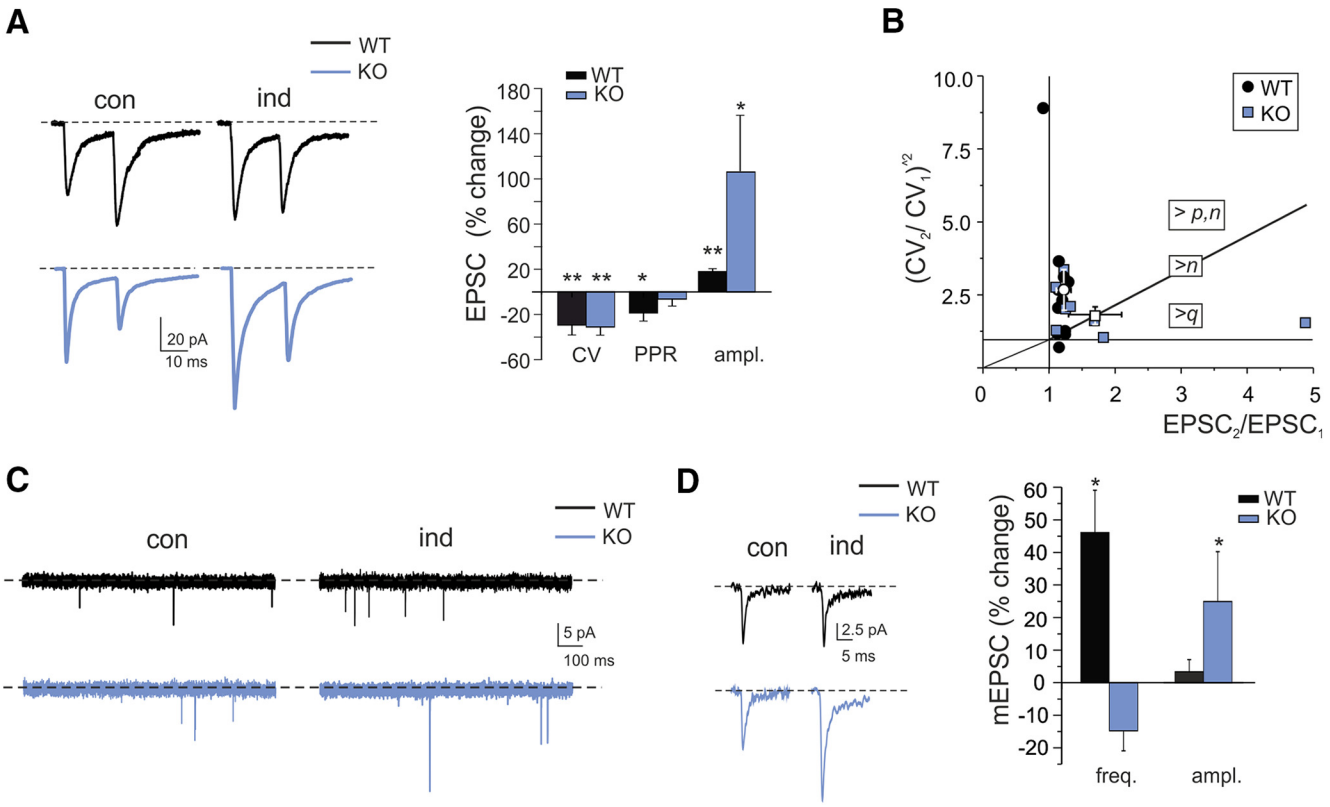

Figure 8. Mechanisms of LTP expression. ***A***, $EPSC_{AMPA}$ in WT and IB2 KO granule cells (average of 30 tracings in both cases) recorded in controls and 20 min after HFS using paired-pulse stimulation (interstimulus interval, 20 ms). The histogram shows the CV, PPR, and $EPSC_{AMPA}$ amplitude changes following HFS in WT and IB2 KO mice. Data are reported as the mean ± SEM. $*p < 0.05$, $**p < 0.01$. ***B***, The $(CV_2/CV_1)^{-2}$ vs $(EPSC_2/EPSC_1)$ plot shows that WT LTP points fall in the sector of increased quantal release (>*p*, *n*), while IB2 KO points fall on the diagonal (>*n*) and in the sector of increased quantum size (>*q*). ***C***, The traces show spontaneous synaptic activity before and after LTP induction in WT and IB2 KO granule cells. Following LTP induction, mEPSC frequency, but not amplitude, increased in WT mice, while mEPSC amplitude, but not frequency, increased in IB2 KO mice. ***D***, Examples of individual mEPSCs before and after LTP induction in WT and IB2 KO granule cells. The histograms compare changes in mEPSC frequency and amplitude during LTP in WT and IB2 KO mice. Data are reported as mean ± SEM. $*p < 0.05$.

In aggregate, these results confirm that LTP in wild-type mice depends almost exclusively on increased neurotransmitter release probability (>*p*) and suggest that LTP in IB2 KO mice rests on a more complex mechanism, including both changes in quantum content (>*p*, *n*) and quantum size (>*q*).

Altered spatial distribution of LTP and LTD in the granular layer of IB2 KO mice

Given the enhanced LTP magnitude (compare Fig. 5) and the altered C/S organization in the IB2 KO granular layer (compare Fig. 3), VSDi experiments were conducted to unravel possible alterations in the spatial distribution of LTP and LTD in the IB2 KO granular layer. As recently shown using the same technique, the spatial distribution of areas undergoing LTP and LTD in the cerebellar granular layer displays a C/S-like organization, with LTP in the core and LTD in the surround (Gandolfi et al., 2015). The investigation of this feature in the WT granular layer revealed a similar organization. Interestingly, the C/S organization of core-LTP and surround-LTD in IB2 KO granular layers showed a shape alteration, with larger LTP cores and thinner LTD surrounds (Fig. 9). The analysis of the granular layer areas with LTP and LTD revealed several abnormalities with respect to WT, as follows: (1) LTP magnitude in the center was higher (WT = 28.4 ± 3.3% vs IB2 KO = 109.4 ± 6.7%; $n = 6$ for both; $p = 8 \times 10^{-6}$); (2) LTP total area underwent an impressive increase (WT = 3.3 ± 1.5% vs IB2 KO = 10.2 ± 3.3%; $n = 6$ for both; $p = 0.047$); (3) LTD total area and magnitude were decreased (total LTD area: WT = 91.4 ± 1.9% vs IB2 KO = 81.3 ± 3.7%; $n = 6$ for both; $p = 0.037$; total LTD magnitude: WT = −34.9 ± 2.8% vs IB2 KO = −24.9 ± 2.6%; $n = 6$ for both; $p = 0.0026$); and (4) the C/S shape showed a significant change in favor of LTP. In particular, the LTP-center was broader in IB2 KO compared with WT (core diameter: WT = 8.4 ± 0.7 μm vs IB2 KO = 32.0 ± 4.1 μm; $n = 6$, respectively; $p = 0.0005$), and the LTD in the surround was less deep (WT = −37.3 ± 1.5% vs IB2 KO = −22.0 ± 2.5%; $n = 6$ for both; $p = 0.0004$; Fig. 9*C*,*D*).

Discussion

The main observation of this article is that profound alterations in signal processing occur at the input stage of cerebellum in an ASD model, the IB2 KO mouse. Intrinsic excitability, synaptic transmission, and synaptic plasticity in granule cells were enhanced in the absence of apparent compensation by the inhibitory circuit, causing a net increase in E/I balance. This in turn changed the spatial organization of neuronal responses, such that the core in C/S structures predominated over the inhibitory surround and LTP spread over larger areas.

Granule cell hyperfunctioning and the NMDA receptor-dependent current

In IB2 KO mice, cerebellar granule cells were hyperfunctioning. Enhanced synaptic transmission appeared as a 2.4 times larger spike emission in response to high-frequency input bursts and was clearly correlated with larger NMDA receptor-mediated currents and increased intrinsic excitability. Enhanced intrinsic excitability appeared as a 2.1–7.1 (depending on current injection)

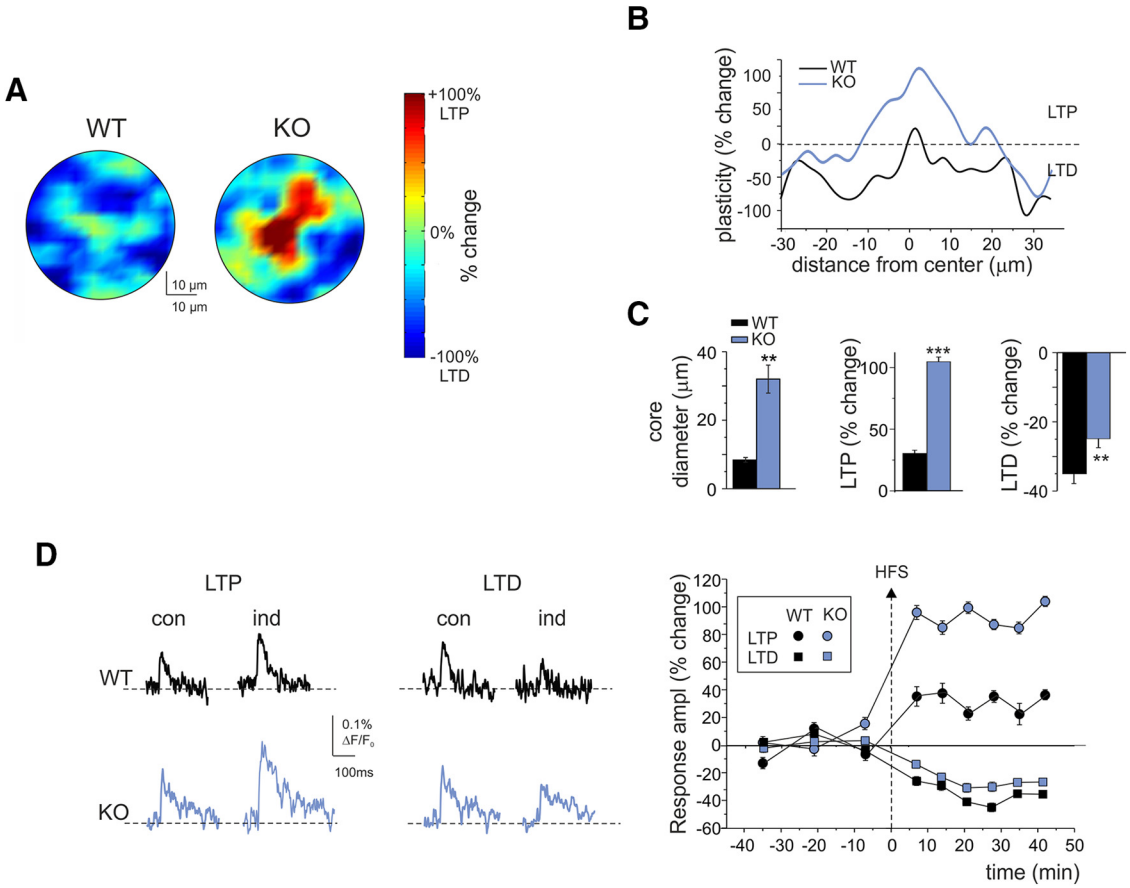

Figure 9. Spatial distribution of the long-term plasticity of granular layer responses to mossy fiber stimulation. ***A***, VSDi normalized maps showing the spatial distribution of LTP and LTD in WT and IB2 KO granular layers (average of 6 recordings in both cases). ***B***, The plot shows plasticity as a function of distance from the center for the maps shown in ***A***. Note that in IB2 KO granular layers the LTP magnitude in the core is larger, and that the core is broader than that in WT granular layers. ***C***, The histograms show, in WT and IB2 KO mice, the average core diameter and the LTP and LTD amplitudes 30 min after HFS ($n = 6$ for both). Note that the IB2 KO granular layer shows larger LTP, smaller LTD, and larger cores than the WT granular layer. Data are reported as the mean ± SEM. $^{***}p < 0.001$; $^{**}p < 0.01$. ***D***, VSDi recordings showing LTP and LTD of granular layer responses to mossy fiber stimulation. Exemplar traces before and 30 min after the induction protocol are reported for WT and IB2 KO granular layers. The plot shows the average time course of LTP and LTD for WT and IB2 KO granular layers ($n = 6$ for both). Data are reported as the mean ± SEM.

higher efficiency in generating spikes during current injection and was correlated with larger Na^+ and K^+ membrane currents. Enhanced synaptic plasticity manifested as a 5.3 times larger LTP compared with that normally measured at the mossy fiber–granule cell synapse (Prestori et al., 2008, 2013). While normal LTP is almost entirely sustained by increased neurotransmitter release probability (Sola et al., 2004; D'Errico et al., 2009), IB2 KO LTP was expressed through a compound presynaptic and postsynaptic mechanism. This was consistently indicated by the increase in minis amplitude ($>q$) and a decrease in EPSC PPR ($>n, p$) and was confirmed by the ubiquitous distribution of points in the $(CV_2/CV_1)^{-2}$ versus (M_2/M_1) plot. The intervention of a postsynaptic expression mechanism was key to explaining the neurotransmission increase in IB2 KO mice granule cells (~120%), which exceeds the theoretical limit of presynaptic expression alone (~60%; Sola et al., 2004).

Interestingly, the whole set of alterations was likely to reflect, directly or indirectly, the NMDA receptor-mediated current enhancement occurring at the mossy fiber–granule cell synapse. In IB2 KO mice, the NMDA synaptic current of granule cells was increased by ~2.5 times, as anticipated in the study by Giza et al. (2010), while the AMPA receptor-mediated current was unaltered. During bursts, the granule cell NMDA current is known to exert a strong depolarizing action entraining a regenerative cycle (D'Angelo et al., 2005), in which depolarization removes NMDA channel unblock, further increasing the NMDA current. The combination of this effect with enhanced intrinsic excitability could easily explain the enhanced synaptic transmission characterizing IB2 KO granule cells. In turn, enhanced NMDA receptor activation could also promote stronger plasticity of synaptic transmission and intrinsic excitability (Armano et al., 2000; Gall et al., 2005). An enhanced tonic NMDA receptor activation (Rossi et al., 2002) could also increase intrinsic excitability, possibly through facilitated NMDA receptor activation by ambient extracellular glutamate (Sah et al., 1989; Nieus et al., 2006; Le Meur et al., 2007) regulating intracellular cascades and ionic voltage-dependent mechanisms (Cohen et al., 1996; Jugloff et al., 2000; Marks and Fadool, 2007; Mulholland et al., 2008).

Functional alterations of the granular layer microcircuit

Given the absence of changes in synaptic inhibition, the enhancements in excitatory synaptic transmission and intrinsic excitability provide an explanation for the remarkable increase in E/I balance, for the prevalence of core over surround in C/S responses, and for the extension of the LTP territory. The C/S organization of the cerebellum granular layer depends on the balance between granule cell excitation and Golgi cell inhibition (Mapelli and D'Angelo, 2007). Here, the strong enhancement of the NMDA current could effectively counteract inhibition (Nieus et al., 2014) extending the core and changing the C/S from the

Mexican hat to the stovepipe hat shape. The elevated input resistance and intrinsic excitability of IB2 KO granule cells could collaborate with elevated NMDA receptor-dependent transmission to spatially expand the excitatory footprint and zone of LTP. The consequences of NMDA receptor hyperfunctioning on the E/I balance and C/S changes could be further analyzed using realistic mathematical models of the granular layer (Solinas et al., 2010; Sudhakar et al., 2017).

NMDA receptor expression in granule cells is the strongest of cerebellum (Monaghan and Cotman, 1985) and is reasonable to speculate that damage there could have a high impact on ASD pathogenesis. Although granular layer circuit alterations were uncompensated leading to a net E/I increase, some changes downstream might have a compensatory meaning. For example, in IB2 KO mice, the thinner molecular layer, the simplified dendritic tree, and the smaller climbing fiber responses of Purkinje cells (Giza et al., 2010) may limit the impact of granular layer overexcitation. Another effect that might be compensatory is the emergence of an NMDA receptor-independent form of mossy fiber–granule cell LTD, which might help to counterbalance the excess LTP at the same synapse when $GABA_A$ receptor-dependent inhibition is engaged (Fig. 7).

Comparison of alterations with other circuits and ASD models

The alterations observed in the cerebellum granular layer of IB2 KO mice resemble in some respects those observed in other brain structures of ASD mice. An enhanced NMDA receptor-mediated neurotransmission was proposed to cause hyper-reactivity and hyperplasticity in the somatosensory cortex (Rinaldi et al., 2007, 2008a), in pyramidal neurons of the medium prefrontal cortex (Rinaldi et al., 2008b), and in the amygdala (Markram et al., 2008). Interestingly, hyper-reactivity and hyperplasticity were correlated with enhanced E/I balance in relation to enhanced NMDA receptor-mediated neurotransmission (Markram et al., 2008). Therefore, our results support the concept that enhanced NMDA receptor-mediated neurotransmission is a common bottleneck for ASD pathogenesis in different brain areas, including the cerebellum. The change of C/S shape from Mexican hat to stovepipe hat is especially interesting in view of the ASD hypothesis developed for cortical minicolumns, the fundamental module of the neocortex (Casanova et al., 2002, 2006; Hutsler and Casanova, 2016). The histological analysis postmortem of minicolumns in ASD patients has revealed reduced size and altered neuronal organization, suggesting that lateral inhibition was reduced. In the C/S of the cerebellum granular layer, the effectiveness of lateral inhibition was indeed reduced by the increased intensity and extension of the excitation core. Therefore, a reduced effectiveness of the surround inhibition of cortical and cerebellar modules may be a common trait of the disease in different brain microcircuits. The picture may be complicated by the interactions among causative, compensatory, and developmental factors. For example, in *Gabrb3* mutants, an increased metabotropic glutamate receptor activation in deep cerebellar nuclei has been proposed to prevent the downstream propagation of effects and to protect from ASD in males (Mercer et al., 2016).

Possible consequences of alterations on cerebellar functioning

The cerebellar granular layer has been proposed to perform expansion recoding and spatial pattern separation of input signals (Marr, 1969), which can be regulated by long-term synaptic plasticity at the mossy fiber–granule cell relay (Hansel et al., 2001; D'Angelo and De Zeeuw, 2009; D'Angelo, 2014). In IB2 KO mice, mossy fiber burst retransmission was enhanced, and the effect could be further amplified by LTP (Nieus et al., 2006). Moreover, the excited areas were broader and poorly limited by surround inhibition. Therefore, in the granular layer microcircuit, expansion recoding and spatial pattern separation could be compromised. Moreover, IB2 KO mice showed a delayed transmission at the climbing fiber–Purkinje cell synapse (Giza et al., 2010). Altogether, these alterations could alter coincidence detection and deregulate LTD at parallel fiber–Purkinje cell synapses (Koekkoek et al., 2005; Baudouin et al., 2012; Piochon et al., 2014, 2016; Peter et al., 2016). These functional modifications might impair the processes of novelty detection and attention switching (D'Angelo and Casali, 2013) toward new environmental or internal cues normally performed by associative areas (especially prefrontal), contributing to generate the combination of cerebellar and ASD symptoms presented by IB2 KO mice.

Conclusions

The complex derangement of signal processing and plasticity in the cerebellum granular layer of IB2 KO mice supports a causative role of cerebellum in ASD pathogenesis. NMDA receptor dependence and microcircuit alterations resembled the hallmarks reported for cortical minicolumns, including synaptic hyper-reactivity, synaptic hyperplasticity, increased E/I balance, and C/S changes. In the cerebellum, these alterations may play a crucial role in generating ASDs as well as motor symptoms. The cerebellum forms multiple closed-loop circuits with cerebral cortical regions that underlie movement, attention, language, social processing, and executive control (Snider and Eldred, 1951; Middleton and Strick, 2000; Habas et al., 2009; Strick et al., 2009; Kellermann et al., 2012; D'Angelo and Casali, 2013; Sokolov et al., 2014; Palesi et al., 2017), providing the anatomical substrate by which cerebellar dysfunction could contribute to ASDs (Schmahmann, 2004, 2010; Schmahmann et al., 2007; D'Angelo and Casali, 2013; Rogers et al., 2013; D'Mello and Stoodley, 2015; Stoodley et al., 2017). Future neuroimaging studies may be used to localize cerebellar activation in ASDs (Stoodley et al., 2017), determining how cerebellar abnormalities combine with those occurring in other brain regions (Bolduc and Limperopoulos, 2009; Limperopoulos et al., 2009; Bolduc et al., 2011; Wang et al., 2014; Hampson and Blatt, 2015; Mosconi et al., 2015).

References

Allen G (2006) Cerebellar contributions to autism spectrum disorders. Clin Neurosci Res 6:195–207.

Amaral DG (2011) The promise and the pitfalls of autism research: an introductory note for new autism researchers. Brain Res 1380:3–9.

Armano S, Rossi P, Taglietti V, D'Angelo E (2000) Long-term potentiation of intrinsic excitability at the mossy fiber-granule cell synapse of rat cerebellum. J Neurosci 20:5208–5216.

Banerjee S, Riordan M, Bhat MA (2014) Genetic aspects of autism spectrum disorders: insights from animal models. Front Cell Neurosci 8:58.

Bardoni R, Belluzzi O (1994) Modifications of A-current kinetics in mammalian central neurones induced by extracellular zinc. J Physiol 479:389–400.

Baudouin SJ, Gaudias J, Gerharz S, Hatstatt L, Zhou K, Punnakkal P, Tanaka KF, Spooren W, Hen R, De Zeeuw CI, Vogt K, Scheiffele P (2012) Shared synaptic pathophysiology in syndromic and nonsyndromic rodent models of autism. Science 338:128–132.

Bekkers JM, Stevens CF (1990) Presynaptic mechanism for long-term potentiation in the hippocampus. Nature 346:724–729.

Betancur C (2011) Etiological heterogeneity in autism spectrum disorders: more than 100 genetic and genomic disorders and still counting. Brain Res 1380:42–77.

Bolduc ME, Limperopoulos C (2009) Neurodevelopmental outcomes in children with cerebellar malformations: a systematic review. Dev Med Child Neurol 51:256–267.

Bolduc ME, Du Plessis AJ, Sullivan N, Khwaja OS, Zhang X, Barnes K, Robertson RL, Limperopoulos C (2011) Spectrum of neurodevelopmental disabilities in children with cerebellar malformations. Dev Med Child Neurol 53:409–416.

Brickley SG, Cull-Candy SG, Farrant M (1996) Development of a tonic form of synaptic inhibition in rat cerebellar granule cells resulting from persistent activation of GABAA receptors. J Physiol 497:753–759.

Broussard DM (2014) The cerebellum: learning movement, language, and social skills. Chichester, UK: Wiley.

Casanova MF (2003) Modular concepts of brain organization and the neuropathology of psychiatric conditions. Psychiatry Res 118:101–102.

Casanova MF (2006) Neuropathological and genetic findings in autism: the significance of a putative minicolumnopathy. Neuroscientist 12:435–441.

Casanova MF, Buxhoeveden DP, Brown C (2002) Clinical and macroscopic correlates of minicolumnar pathology in autism. J Child Neurol 17:692–695.

Casanova MF, van Kooten IA, Switala AE, van Engeland H, Heinsen H, Steinbusch HW, Hof PR, Trippe J, Stone J, Schmitz C (2006) Minicolumnar abnormalities in autism. Acta Neuropathol 112:287–303.

Cathala L, Brickley S, Cull-Candy S, Farrant M (2003) Maturation of EPSCs and intrinsic membrane properties enhances precision at a cerebellar synapse. J Neurosci 23:6074–6085.

Cesana E, Pietrajtis K, Bidoret C, Isope P, D'Angelo E, Dieudonné S, Forti L (2013) Granule cell ascending axon excitatory synapses onto Golgi cells implement a potent feedback circuit in the cerebellar granular layer. J Neurosci 33:12430–12446.

Cohen NA, Brenman JE, Snyder SH, Bredt DS (1996) Binding of the inward rectifier K+ channel kir 2.3 to PSD-95 is regulated by protein kinase A phosphorylation. Neuron 17:759–767.

Courchesne E, Allen G (1997) Prediction and preparation, fundamental functions of the cerebellum. Learn Mem 4:1–35.

Curatolo P, Ben-Ari Y, Bozzi Y, Catania MV, D'Angelo E, Mapelli L, Oberman LM, Rosenmund C, Cherubini E (2014) Synapses as therapeutic targets for autism spectrum disorders: an international symposium held in Pavia on july 4th, 2014. Front Cell Neurosci 8:309.

D'Angelo E (2014) The organization of plasticity in the cerebellar cortex: from synapses to control. Prog Brain Res 210:31–58.

D'Angelo E, Casali S (2013) Seeking a unified framework for cerebellar function and dysfunction: from circuit operations to cognition. Front Neural Circuits 6:116.

D'Angelo E, De Zeeuw CI (2009) Timing and plasticity in the cerebellum: focus on the granular layer. Trends Neurosci 32:30–40.

D'Angelo E, De Filippi G, Rossi P, Taglietti V (1995) Synaptic excitation of individual rat cerebellar granule cells in situ: evidence for the role of NMDA receptors. J Physiol 484:397–413.

D'Angelo E, De Filippi G, Rossi P, Taglietti V (1998) Ionic mechanism of electroresponsiveness in cerebellar granule cells implicates the action of a persistent sodium current. J Neurophysiol 80:493–503.

D'Angelo E, Rossi P, Armano S, Taglietti V (1999) Evidence for NMDA and mGlu receptor-dependent long-term potentiation of mossy fiber-granule cell transmission in rat cerebellum. J Neurophysiol 81:277–287.

D'Angelo E, Rossi P, Gall D, Prestori F, Nieus T, Maffei A, Sola E (2005) Long-term potentiation of synaptic transmission at the mossy fiber-granule cell relay of cerebellum. Prog Brain Res 148:69–80.

D'Errico A, Prestori F, D'Angelo E (2009) Differential induction of bidirectional long-term changes in neurotransmitter release by frequency-coded patterns at the cerebellar input. J Physiol 587:5843–5857.

De Rubeis S, Buxbaum JD (2015) Genetics and genomics of autism spectrum disorder: embracing complexity. Hum Mol Genet 24:R24–R31.

D'Mello AM, Stoodley CJ (2015) Cerebro-cerebellar circuits in autism spectrum disorder. Front Neurosci 9:408.

Ellegood J, Anagnostou E, Babineau BA, Crawley JN, Lin L, Genestine M, DiCicco-Bloom E, Lai JK, Foster JA, Peñagarikano O, Geschwind DH, Pacey LK, Hampson DR, Laliberté CL, Mills AA, Tam E, Osborne LR, Kouser M, Espinosa-Becerra F, Xuan Z, et al. (2015) Clustering autism: using neuroanatomical differences in 26 mouse models to gain insight into the heterogeneity. Mol Psychiatry 20:118–125.

Gall D, Prestori F, Sola E, D'Errico A, Roussel C, Forti L, Rossi P, D'Angelo E (2005) Intracellular calcium regulation by burst discharge determines bidirectional long-term synaptic plasticity at the cerebellum input stage. J Neurosci 25:4813–4822.

Gandolfi D, Pozzi P, Tognolina M, Chirico G, Mapelli J, D'Angelo E (2014) The spatiotemporal organization of cerebellar network activity resolved by two-photon imaging of multiple single neurons. Front Cell Neurosci 8:92.

Gandolfi D, Mapelli J, D'Angelo E (2015) Long-term spatiotemporal reconfiguration of neuronal activity revealed by voltage-sensitive dye imaging in the cerebellar granular layer. Neural Plast 2015:284986.

Giza J, Urbanski MJ, Prestori F, Bandyopadhyay B, Yam A, Friedrich V, Kelley K, D'Angelo E, Goldfarb M (2010) Behavioral and cerebellar transmission deficits in mice lacking the autism-linked gene islet brain-2. J Neurosci 30:14805–14816.

Gogolla N, Leblanc JJ, Quast KB, Südhof TC, Fagiolini M, Hensch TK (2009) Common circuit defect of excitatory-inhibitory balance in mouse models of autism. J Neurodev Disord 1:172–181.

Habas C, Kamdar N, Nguyen D, Prater K, Beckmann CF, Menon V, Greicius MD (2009) Distinct cerebellar contributions to intrinsic connectivity networks. J Neurosci 29:8586–8594.

Hampson DR, Blatt GJ (2015) Autism spectrum disorders and neuropathology of the cerebellum. Front Neurosci 9:420.

Hansel C, Linden DJ, D'Angelo E (2001) Beyond parallel fiber LTD: the diversity of synaptic and non-synaptic plasticity in the cerebellum. Nat Neurosci 4:467–475.

Hutsler JJ, Casanova MF (2016) Review: cortical construction in autism spectrum disorder: columns, connectivity and the subplate. Neuropathol Appl Neurobiol 42:115–134.

Ito M (2008) Control of mental activities by internal models in the cerebellum. Nat Rev Neurosci 9:304–313.

Jugloff DG, Khanna R, Schlichter LC, Jones OT (2000) Internalization of the Kv1.4 potassium channel is suppressed by clustering interactions with PSD-95. J Biol Chem 275:1357–1364.

Kellermann T, Regenbogen C, De Vos M, Moßnang C, Finkelmeyer A, Habel U (2012) Effective connectivity of the human cerebellum during visual attention. J Neurosci 32:11453–11460.

Kim H, Lim CS, Kaang BK (2016) Neuronal mechanisms and circuits underlying repetitive behaviors in mouse models of autism spectrum disorder. Behav Brain Funct 12:3.

Kloth AD, Badura A, Li A, Cherskov A, Connolly SG, Giovannucci A, Bangash MA, Grasselli G, Peñagarikano O, Piochon C, Tsai PT, Geschwind DH, Hansel C, Sahin M, Takumi T, Worley PF, Wang SS (2015) Cerebellar associative sensory learning defects in five mouse autism models. Elife 4:e06085.

Koekkoek SK, Yamaguchi K, Milojkovic BA, Dortland BR, Ruigrok TJ, Maex R, De Graaf W, Smit AE, VanderWerf F, Bakker CE, Willemsen R, Ikeda T, Kakizawa S, Onodera K, Nelson DL, Mientjes E, Joosten M, De Schutter E, Oostra BA, Ito M, et al. (2005) Deletion of FMR1 in purkinje cells enhances parallel fiber LTD, enlarges spines, and attenuates cerebellar eyelid conditioning in fragile X syndrome. Neuron 47:339–352.

Kolevzon A, Angarita B, Bush L, Wang AT, Frank Y, Yang A, Rapaport R, Saland J, Srivastava S, Farrell C, Edelmann LJ, Buxbaum JD (2014) Phelan-McDermid syndrome: a review of the literature and practice parameters for medical assessment and monitoring. J Neurodev Disord 6:39.

Kullmann DM, Nicoll RA (1992) Long-term potentiation is associated with increases in quantal content and quantal amplitude. Nature 357:240–244.

Le Meur K, Galante M, Angulo MC, Audinat E (2007) Tonic activation of NMDA receptors by ambient glutamate of non-synaptic origin in the rat hippocampus. J Physiol 580:373–383.

Limperopoulos C, Robertson RL, Sullivan NR, Bassan H, du Plessis AJ (2009) Cerebellar injury in term infants: clinical characteristics, magnetic resonance imaging findings, and outcome. Pediatr Neurol 41:1–8.

Maffei A, Prestori F, Rossi P, Taglietti V, D'Angelo E (2002) Presynaptic current changes at the mossy fiber-granule cell synapse of cerebellum during LTP. J Neurophysiol 88:627–638.

Maffei A, Prestori F, Shibuki K, Rossi P, Taglietti V, D'Angelo E (2003) NO enhances presynaptic currents during cerebellar mossy fiber-granule cell LTP. J Neurophysiol 90:2478–2483.

Magistretti J, Castelli L, Forti L, D'Angelo E (2006) Kinetic and functional analysis of transient, persistent and resurgent sodium currents in rat cerebellar granule cells in situ: an electrophysiological and modelling study. J Physiol 573:83–106.

Malgaroli A, Ting AE, Wendland B, Bergamaschi A, Villa A, Tsien RW, Scheller RH (1995) Presynaptic component of long-term potentiation visualized at individual hippocampal synapses. Science 268:1624–1628.

Malinow R, Tsien RW (1990) Presynaptic enhancement shown by whole-cell recordings of long-term potentiation in hippocampal slices. Nature 346:177–180.

Manabe T, Wyllie DJ, Perkel DJ, Nicoll RA (1993) Modulation of synaptic transmission and long-term potentiation: effects on paired pulse facilitation and EPSC variance in the CA1 region of the hippocampus. J Neurophysiol 70:1451–1459.

Manning MA, Cassidy SB, Clericuzio C, Cherry AM, Schwartz S, Hudgins L, Enns GM, Hoyme HE (2004) Terminal 22q deletion syndrome: a newly recognized cause of speech and language disability in the autism spectrum. Pediatrics 114:451–457.

Mapelli J, D'Angelo E (2007) The spatial organization of long-term synaptic plasticity at the input stage of cerebellum. J Neurosci 27:1285–1296.

Mapelli J, Gandolfi D, D'Angelo E (2010) Combinatorial responses controlled by synaptic inhibition in the cerebellum granular layer. J Neurophysiol 103:250–261.

Mapelli L, Rossi P, Nieus T, D'Angelo E (2009) Tonic activation of GABAB receptors reduces release probability at inhibitory connections in the cerebellar glomerulus. J Neurophysiol 101:3089–3099.

Mapelli L, Solinas S, D'Angelo E (2014) Integration and regulation of glomerular inhibition in the cerebellar granular layer circuit. Front Cell Neurosci 8:55.

Markram K, Markram H (2010) The intense world theory—a unifying theory of the neurobiology of autism. Front Hum Neurosci 4:224.

Markram K, Rinaldi T, La Mendola D, Sandi C, Markram H (2008) Abnormal fear conditioning and amygdala processing in an animal model of autism. Neuropsychopharmacology 33:901–912.

Marks DR, Fadool DA (2007) Post-synaptic density perturbs insulin-induced Kv1.3 channel modulation via a clustering mechanism involving the SH3 domain. J Neurochem 103:1608–1627.

Marr D (1969) A theory of cerebellar cortex. J Physiol 202:437–470.

Mercer AA, Palarz KJ, Tabatadze N, Woolley CS, Raman IM (2016) Sex differences in cerebellar synaptic transmission and sex-specific responses to autism-linked Gabrb3 mutations in mice. Elife 5:e07596.

Middleton FA, Strick PL (2000) Basal ganglia and cerebellar loops: motor and cognitive circuits. Brain Res Brain Res Rev 31:236–250.

Mitchell SJ, Silver RA (2000) Glutamate spillover suppresses inhibition by activating presynaptic mGluRs. Nature 404:498–502.

Mitchell SJ, Silver RA (2003) Shunting inhibition modulates neuronal gain during synaptic excitation. Neuron 38:433–445.

Monaghan DT, Cotman CW (1985) Distribution of *N*-methyl-D-aspartate-sensitive L-[3H]glutamate-binding sites in rat brain. J Neurosci 5:2909–2919.

Mosconi MW, Wang Z, Schmitt LM, Tsai P, Sweeney JA (2015) The role of cerebellar circuitry alterations in the pathophysiology of autism spectrum disorders. Front Neurosci 9:296.

Mulholland PJ, Carpenter-Hyland EP, Hearing MC, Becker HC, Woodward JJ, Chandler LJ (2008) Glutamate transporters regulate extrasynaptic NMDA receptor modulation of $K_v2.1$ potassium channels. J Neurosci 28:8801–8809.

Nieus TR, Mapelli L, D'Angelo E (2014) Regulation of output spike patterns by phasic inhibition in cerebellar granule cells. Front Cell Neurosci 8:246.

Nieus T, Sola E, Mapelli J, Saftenku E, Rossi P, D'Angelo E (2006) LTP regulates burst initiation and frequency at mossy fiber-granule cell synapses of rat cerebellum: experimental observations and theoretical predictions. J Neurophysiol 95:686–699.

Palesi F, De Rinaldis A, Castellazzi G, Calamante F, Muhlert N, Chard D, Tournier JD, Magenes G, D'Angelo E, Gandini Wheeler-Kingshott CAM (2017) Contralateral cortico-ponto-cerebellar pathways reconstruction in humans in vivo: implications for reciprocal cerebro-cerebellar structural connectivity in motor and non-motor areas. Sci Rep 7:12841.

Peter S, Ten Brinke MM, Stedehouder J, Reinelt CM, Wu B, Zhou H, Zhou K, Boele HJ, Kushner SA, Lee MG, Schmeisser MJ, Boeckers TM, Schonewille M, Hoebeek FE, De Zeeuw CI (2016) Dysfunctional cerebellar purkinje cells contribute to autism-like behaviour in Shank2-deficient mice. Nat Commun 7:12627.

Phelan MC, Rogers RC, Saul RA, Stapleton GA, Sweet K, McDermid H, Shaw SR, Claytor J, Willis J, Kelly DP (2001) 22q13 deletion syndrome. Am J Med Genet 101:91–99.

Piochon C, Kloth AD, Grasselli G, Titley HK, Nakayama H, Hashimoto K, Wan V, Simmons DH, Eissa T, Nakatani J, Cherskov A, Miyazaki T, Watanabe M, Takumi T, Kano M, Wang SS, Hansel C (2014) Cerebellar plasticity and motor learning deficits in a copy-number variation mouse model of autism. Nat Commun 5:5586.

Piochon C, Kano M, Hansel C (2016) LTD-like molecular pathways in developmental synaptic pruning. Nat Neurosci 19:1299–1310.

Prestori F, Rossi P, Bearzatto B, Lainé J, Necchi D, Diwakar S, Schiffmann SN, Axelrad H, D'Angelo E (2008) Altered neuron excitability and synaptic plasticity in the cerebellar granular layer of juvenile prion protein knockout mice with impaired motor control. J Neurosci 28:7091–7103.

Prestori F, Bonardi C, Mapelli L, Lombardo P, Goselink R, De Stefano ME, Gandolfi D, Mapelli J, Bertrand D, Schonewille M, De Zeeuw C, D'Angelo E (2013) Gating of long-term potentiation by nicotinic acetylcholine receptors at the cerebellum input stage. PLoS One 8:e64828.

Qiu S, Aldinger KA, Levitt P (2012) Modeling of autism genetic variations in mice: focusing on synaptic and microcircuit dysfunctions. Dev Neurosci 34:88–100.

Rinaldi T, Kulangara K, Antoniello K, Markram H (2007) Elevated NMDA receptor levels and enhanced postsynaptic long-term potentiation induced by prenatal exposure to valproic acid. Proc Natl Acad Sci U S A 104:13501–13506.

Rinaldi T, Silberberg G, Markram H (2008a) Hyperconnectivity of local neocortical microcircuitry induced by prenatal exposure to valproic acid. Cereb Cortex 18:763–770.

Rinaldi T, Perrodin C, Markram H (2008b) Hyper-connectivity and hyper-plasticity in the medial prefrontal cortex in the valproic acid animal model of autism. Front Neural Circuits 2:4.

Rogers TD, Dickson PE, McKimm E, Heck DH, Goldowitz D, Blaha CD, Mittleman G (2013) Reorganization of circuits underlying cerebellar modulation of prefrontal cortical dopamine in mouse models of autism spectrum disorder. Cerebellum 12:547–556.

Rossi P, De Filippi G, Armano S, Taglietti V, D'Angelo E (1998) The weaver mutation causes a loss of inward rectifier current regulation in premigratory granule cells of the mouse cerebellum. J Neurosci 18:3537–3547.

Rossi P, Sola E, Taglietti V, Borchardt T, Steigerwald F, Utvik JK, Ottersen OP, Köhr G, D'Angelo E (2002) NMDA receptor 2 (NR2) C-terminal control of NR open probability regulates synaptic transmission and plasticity at a cerebellar synapse. J Neurosci 22:9687–9697.

Rubenstein JL, Merzenich MM (2003) Model of autism: increased ratio of excitation/inhibition in key neural systems. Genes Brain Behav 2:255–267.

Sah P, Hestrin S, Nicoll RA (1989) Tonic activation of NMDA receptors by ambient glutamate enhances excitability of neurons. Science 246:815–818.

Saviane C, Silver RA (2006) Errors in the estimation of the variance: implications for multiple-probability fluctuation analysis. J Neurosci Methods 153:250–260.

Schmahmann JD (2004) Disorders of the cerebellum: ataxia, dysmetria of thought, and the cerebellar cognitive affective syndrome. J Neuropsychiatry Clin Neurosci 16:367–378.

Schmahmann JD (2010) The role of the cerebellum in cognition and emotion: personal reflections since 1982 on the dysmetria of thought hypothesis, and its historical evolution from theory to therapy. Neuropsychol Rev 20:236–260.

Schmahmann JD, Weilburg JB, Sherman JC (2007) The neuropsychiatry of the cerebellum- insights from the clinic. Cerebellum 6:254–267.

Sgritta M, Locatelli F, Soda T, Prestori F, D'Angelo EU (2017) Hebbian spike-timing dependent plasticity at the cerebellar input stage. J Neurosci 37:2809–2823.

Sharma G, Vijayaraghavan S (2003) Modulation of presynaptic store calcium induces release of glutamate and postsynaptic firing. Neuron 38:929–939.

Silver RA, Cull-Candy SG, Takahashi T (1996) Non-NMDA glutamate receptor occupancy and open probability at a rat cerebellar synapse with single and multiple release sites. J Physiol 494:231–250.

Snider R, Eldred E (1951) Electro-anatomical studies on cerebro-cerebellar connections in the cat. J Comp Neurol 95:1–16.

Sokolov AA, Erb M, Grodd W, Pavlova MA (2014) Structural loop between the cerebellum and the superior temporal sulcus: evidence from diffusion tensor imaging. Cereb Cortex 24:626–632.

Sola E, Prestori F, Rossi P, Taglietti V, D'Angelo E (2004) Increased neu-

rotransmitter release during long-term potentiation at mossy fibre-granule cell synapses in rat cerebellum. J Physiol 557:843–861.
Solinas S, Nieus T, D'Angelo E (2010) A realistic large-scale model of the cerebellum granular layer predicts circuit spatio-temporal filtering properties. Front Cell Neurosci 4:12.
Soorya L, Kolevzon A, Zweifach J, Lim T, Dobry Y, Schwartz L, Frank Y, Wang AT, Cai G, Parkhomenko E, Halpern D, Grodberg D, Angarita B, Willner JP, Yang A, Canitano R, Chaplin W, Betancur C, Buxbaum JD (2013) Prospective investigation of autism and genotype-phenotype correlations in 22q13 deletion syndrome and SHANK3 deficiency. Mol Autism 4:18.
Stoodley CJ, D'Mello AM, Ellegood J, Jakkamsetti V, Liu P, Nebel MB, Gibson JM, Kelly E, Meng F, Cano CA, Pascual JM, Mostofsky SH, Lerch JP, Tsai PT (2017) Altered cerebellar connectivity in autism and cerebellar-mediated rescue of autism-related behaviors in mice. Nat Neurosci 20:1744–1751.
Strick PL, Dum RP, Fiez JA (2009) Cerebellum and nonmotor function. Annu Rev Neurosci 32:413–434.
Sudhakar SK, Hong S, Raikov I, Publio R, Lang C, Close T, Guo D, Negrello M, De Schutter E (2017) Spatiotemporal network coding of physiological mossy fiber inputs by the cerebellar granular layer. PLoS Comput Biol 13:e1005754.
Sztainberg Y, Zoghbi HY (2016) Lessons learned from studying syndromic autism spectrum disorders. Nat Neurosci 19:1408–1417.
Tsai PT (2016) Autism and cerebellar dysfunction: evidence from animal models. Semin Fetal Neonatal Med 21:349–355.
Tu S, Akhtar MW, Escorihuela RM, Amador-Arjona A, Swarup V, Parker J, Zaremba JD, Holland T, Bansal N, Holohan DR, Lopez K, Ryan SD, Chan SF, Yan L, Zhang X, Huang X, Sultan A, McKercher SR, Ambasudhan R, Xu H, et al. (2017) NitroSynapsin therapy for a mouse MEF2C haploinsufficiency model of human autism. Nat Commun 8:1488.
Uzunova G, Pallanti S, Hollander E (2016) Excitatory/inhibitory imbalance in autism spectrum disorders: implications for interventions and therapeutics. World J Biol Psychiatry 17:174–186.
Vranesic I, Iijima T, Ichikawa M, Matsumoto G, Knöpfel T (1994) Signal transmission in the parallel fiber-purkinje cell system visualized by high-resolution imaging. Proc Natl Acad Sci U S A 91:13014–13017.
Wang SS, Kloth AD, Badura A (2014) The cerebellum, sensitive periods, and autism. Neuron 83:518–532.
Wyllie DJ, Manabe T, Nicoll RA (1994) A rise in postsynaptic Ca2+ potentiates miniature excitatory postsynaptic currents and AMPA responses in hippocampal neurons. Neuron 12:127–138.
Yang Y, Calakos N (2013) Presynaptic long-term plasticity. Front Synaptic Neurosci 5:8.
Yasuda J, Whitmarsh AJ, Cavanagh J, Sharma M, Davis RJ (1999) The JIP group of mitogen-activated protein kinase scaffold proteins. Mol Cell Biol 19:7245–7254.
Zeidán-Chuliá F, de Oliveira BN, Casanova MF, Casanova EL, Noda M, Salmina AB, Verkhratsky A (2016) Up-regulation of oligodendrocyte lineage markers in the cerebellum of autistic patients: evidence from network analysis of gene expression. Mol Neurobiol 53:4019–4025.
Zucker RS, Regehr WG (2002) Short-term synaptic plasticity. Annu Rev Physiol 64:355–405.